

AD-A111 791

VIRGINIA POLYTECHNIC INST AND STATE UNIV BLACKSBURG --ETC F/6 20/4
COMPUTATION OF HYPERSONIC LAMINAR VISCOUS FLOW OVER A BODY WITH--ETC(U)
MAY 81 M D KIM, C H LEWIS

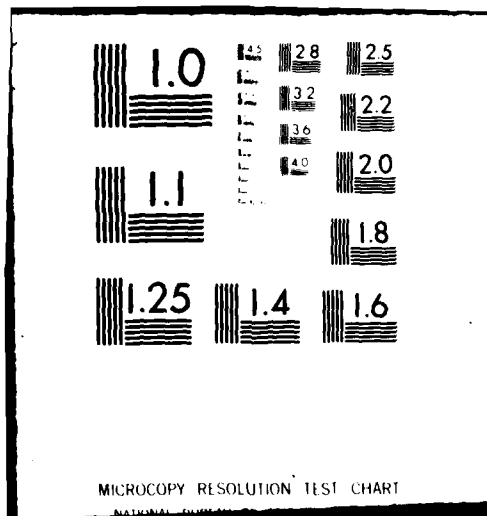
UNCLASSIFIED

NL

1 of 1
All pages



END
DATE
FILMED
4-82
DTIC



ADA111791

COMPUTATION OF HYPERSONIC LAMINAR VISCOUS FLOW OVER A BODY
WITH MASS TRANSFER AND/OR SPIN AT ANGLE OF ATTACK

M. D. KIM^{*} and C. H. LEWIS^{**}

Aerospace and Ocean Engineering Department
Virginia Polytechnic Institute and State University
Blacksburg, Virginia 24061

14 MAY 81

ABSTRACT

Computational results of hypersonic laminar viscous flow over blunt-nosed bodies with mass transfer and/or spin are presented. An implicit-iterative numerical scheme at each marching step is used to solve the parabolized Navier-Stokes equations. The code takes into account the mass-transfer and spin effects in the boundary condition at the body surface and the periodic effect in the boundary condition around the body. To facilitate convergence, the v-momentum equation has been used rather than the continuity equation to provide the pressure at the body boundary. The coupling effects of mass transfer and spin on the integrated forces and moments as well as the surface properties are presented and discussed.

INTRODUCTION

In recent years the analysis of hypersonic viscous flow past reentry vehicles with mass transfer and/or spin has been a problem of considerable interest in ballistics because of its relevance in slowly spinning planetary entry. Previously a numerical method (VSL3D)¹ based on a viscous shock-layer approach was applied to the computation of heat- and mass-transfer effects on three-dimensional viscous shock-layer flows by Murray and Lewis.² The VSL3D method was found to give accurate predictions even at very high altitude because the code takes into account wall and shock slip effects. Another numerical analysis for the mass-transfer effect using the viscous shock-layer theory was given by Whitehead and Davis.³ The VSL3D method has a restriction on the angle of attack for the entire solution around the body. In other words, since the numerical scheme used is parabolic in the circumferential direction, it cannot treat the crossflow separated region. In the above studies, spin effects on the flowfield were not treated.

Recently a numerical approach for the hypersonic viscous flowfield solution was developed by Lubard and Helliwell⁴ using the parabolized Navier-Stokes equations (PNS). The PNS method has been applied to the various

*Graduate Student

**Professor

82 08 09

problems predicting hypersonic viscous flows over bodies at high angles of attack. For instance, Waskiewicz and Lewis⁵ applied the method to a variety of freestream conditions and investigated the limit and applicability of the method. They found that the PNS method could produce accurate predictions of the flowfield during reentry up to at least 38-deg angle of attack. They also discussed the following effects of axial pressure gradient models. For problems involving high Mach number and Reynolds numbers, the implicit gradient model provided unique solutions regardless of the stepsize with no noticeable increase in the number of iterations required for convergence. Problems involving large adverse streamwise pressure gradients due to high angle of attack, large mass transfer, or small Mach and Reynolds numbers can cause difficulties in convergence for the implicit pressure gradient model. In such cases an explicit or zero formulation was needed, and the accuracy of the solution was dependent on the streamwise stepsize. In their work, the VPI VSL3D code was satisfactory for the preparation of an initial plane data which was used to start the PNS solution. In other works, Gogineni and Lewis⁶ reduced the computing times required for an entire solution by combining the VSL3D and PNS methods and also by using a fast implicit-iterative technique known as the Pseudo Elimination Method. The PNS method has been further developed by Helliwell et al.^{7,8} by introducing a more general body-generator coordinate system, thus extending the applicability to more complex bodies. A streamline coordinate system also has been incorporated in the PNS method by Kim and Lewis⁹ in an effort to extend the capability to treat extremely high angles of attack.

Spin effects on the hypersonic viscous flowfields past conical bodies have been computed and analyzed by Agarwal and Rakich.¹⁰ A PNS code has been modified to include the periodic condition for the flow profiles in the windward plane to account for the asymmetry in the flow due to spin. They also introduced a new criterion for defining crossflow separation behind spinning bodies which generalizes the Moore-Rott-Seas criterion for two-dimensional unsteady separation. The onset of separation in the flowfield is characterized by the condition $\partial w / \partial y = 0$ at $w = 0$ where w is the circumferential component of velocity and y the coordinate normal to the body. In their work, detail analyses were made concerning the effects of angle of attack, freestream Reynolds number, nose bluntness, and finally spin rate on the Magnus force components and various flow properties. Coning motion also was considered by Agarwal and Rakich¹¹ using a PNS method further modified. Another study of the spin effects for cones or ogive-cylinder-boattailed bodies has been reported by Sturek and Schiff¹² using another PNS approach. None of the foregoing investigations considered the coupling effects of mass transfer and spin.

In the present study, computational results and discussion are presented for the parametric effects of mass transfer and/or spin together with the reasonable computing times consumed for each test case. The original PNS code used the continuity equation to obtain the wall pressure at the body boundary in the case of mass transfer. Theoretically this method appears quite reasonable because it can provide a finite value of the wall pressure when the normal velocity at wall does not vanish, and moreover it is a relatively simple equation. However, by numerical experiment it has been found that a solution is hardly obtainable by this method in the case of mass transfer. Therefore, in the present work, the v -momentum equation is differentiated to provide the wall pressure at the body boundary. In most cases,

the flowfield solution has been obtained without convergence problems by the current method.

In the next section, the theoretical background and procedure will be presented which includes a discussion of the governing equations, coordinate system, boundary conditions, and numerical solution. A few methods to provide initial plane data are also introduced, and the effect of initial plane data for a starting solution is discussed. In the present work, the zero pressure gradient model has been used for all the test cases in order to obtain a solution in the case of high angles of attack with mass transfer and/or spin.

Two sets of freestream conditions are considered. The first case is $Mach = 5$, $\alpha = 2$ and $Re_{\infty}/ft = 6.21 \times 10^5$. The second case is $Mach = 18$, $\alpha = 15$ and $Re_{\infty}/ft = 5.45 \times 10^5$. For both cases, the body geometry is a spherically blunted 7-deg half-angle cone 0.817-ft long. Spin rates considered are 2000 and 8000 rev/min and mass-transfer rates 0.00125 and 0.00250. For Case 1, an asymmetric sinusoidal distribution of mass transfer around body as well as a constant distribution has been considered. For each freestream condition, computational results were obtained for four parametric cases, i.e., basic case, spin only case, mass transfer only case, and finally mass transfer and spin case. Parametric comparisons are presented to study the effect of mass transfer and/or spin on the Magnus force components as well as all the surface properties. It will be noted that a significant coupling effect on the Magnus force can result from mass transfer and spin. Reasonable computing times required for the solutions are also presented.

ANALYSIS

GOVERNING EQUATIONS

The governing equations are the laminar, steady parabolized Navier-Stokes equations derived by Lubard and Helliwell⁴ under the assumption that the gradients of the shear stress in the streamwise direction are negligibly small compared with the gradients in the direction of normal and circumferential directions. The resulting equations are parabolic in the streamwise direction and elliptic in the crossflow direction. The governing equations include the continuity, three momentum, and energy equations. The fluid density is given by the equation of state for a perfect gas. Prandtl number and specific heat are assumed constant and Sutherland's viscosity law is used.

In addition to the usual boundary-layer order of magnitude terms, $d\phi$ is assumed to be $O(\epsilon)$ to include the crossflow separation and the normal velocity v is taken as $O(1)$. The flow variables are nondimensionalized by their freestream values. The normal coordinate is normalized by the shock-layer thickness to facilitate the computation of the shock location. The complete set of governing equations together with the derivation procedure can be found in Reference 4.

In the development of these equations, a body-oriented coordinate system is used (Figure 1), with x taken along the body generator, y normal to the body surface, and ϕ the circumferential coordinate where $\phi = 0$ represents the windward ray. The coordinate system does not rotate with the body.

BOUNDARY CONDITIONS

The following equations are used for the boundary conditions at the body surface with mass transfer and spin.

$$u = 0$$

$$v = \text{specified distribution (mass transfer)}$$

$$w = \text{specified distribution (spin)}$$

$$h = \text{specified distribution}$$

$$\begin{aligned} \left(\frac{\partial p}{\partial y} \right)_w = & -\frac{1}{r} \frac{\partial(\rho v^2 r)}{\partial y} - \frac{1}{r} \frac{\partial(\rho v w)}{\partial \phi} + \frac{\rho w^2 \cos \theta_c}{r} \\ & + \frac{1}{\text{Re}} \left(\frac{4}{3} \mu \frac{\partial^2 v}{\partial y^2} + \frac{\partial v}{\partial y} \frac{\partial \left(\frac{4}{3} \mu \right)}{\partial y} + \frac{\mu}{r^2} \frac{\partial^2 v}{\partial \phi^2} + \frac{1}{r^2} \frac{\partial v}{\partial \phi} \frac{\partial \mu}{\partial \phi} \right. \\ & \left. + \frac{1}{r} (\mu + \lambda) \frac{\partial^2 w}{\partial \phi \partial y} + \frac{1}{r} \frac{\partial \mu}{\partial \phi} \frac{\partial w}{\partial y} - \frac{1}{r \xi} (\mu + \lambda) \frac{\partial w}{\partial y} \frac{\partial \xi}{\partial \phi} \right) \end{aligned}$$

To obtain the wall pressure for the mass-transfer and spin case, the original code utilized the continuity equation; however, the method turned out to be inefficient for the convergence of a solution by a numerical experiment. It has been found that the employment of the v-momentum equation gives a more stable solution. Thus, for the present analysis the v-momentum equation has been taken and differenced using a one-sided differencing scheme to provide the pressure at the body boundary.

In order to obtain the outer boundary conditions, Rankine-Hugoniot jump conditions are utilized at the shock. The components of freestream velocity in the body oriented coordinate system are:

$$u = \cos \theta_c \cos \alpha - \sin \theta_c \sin \alpha \cos \phi$$

$$v = -\sin \theta_c \cos \alpha - \cos \theta_c \sin \alpha \cos \phi$$

$$w = \sin \phi \sin \alpha$$

From the freestream components and jump conditions, five conservation equations are obtained which can be used to determine the aftershock properties. To uniquely determine the six unknowns ξ , u , v , w , p , h at the shock boundary, one more equation is required. Thus, the one-sided differencing of the continuity equation provides the sixth equation.

Since the windward and leeward surfaces are not symmetry planes for the spinning cone, a periodic condition for the flow profiles in the windward plane is specified, thus providing the boundary conditions in the ϕ -coordinate direction.

In a rectangular y - ϕ grid, the shock may not fall on a mesh point. To resolve this difficulty, a coordinate transformation, $\eta = y/\xi(x, \phi)$ is made, where $\xi(x, \phi)$ is local shock-layer thickness. Due to the coordinate transformation, the shock-layer thickness ξ appears in all the governing equations, thus requiring one more governing equation, $\partial \xi / \partial y = 0$ to be differenced.

INITIAL CONDITIONS

For a numerical flowfield solution which utilizes a marching scheme, preparation of an accurate initial data plane (IDP) is one of the most crucial conditions for a successful start of solution. By previous investigations^{5,6} the viscous shock-layer method (VSL3D)¹ for blunt bodies was found to be able to generate a satisfactory initial data plane to start the PNS solution. Thus, the entire flow properties including the shock shape must be supplied at an initial data plane to get the PNS code started.

Three different methods have been used to generate an initial data plane. The first method is to construct a one-step IDP using the VSL3D method at the sphere-cone juncture. In most cases, the one-step IDP constructed by the VSL3D code was satisfactory to start the PNS solution. The one-step IDP is obtained by an axisymmetric VSL solution and necessary rotations of the solution. In this case, a few initial marching stepsizes should be small to start a solution.

The second method is to prepare a two-step IDP using VSL3D code at any desired axial station of the body. This method is better than the first one for the convergence of the starting solutions, and hence the initial marching step-sizes can be taken larger. The third method is to prepare a two-step IDP using LUB2 code which is another PNS code developed by Agopian et al.⁷ for more general bodies. In this method, an axisymmetric VSL solution provides an IDP at the blunt nose for the LUB2 solution, and then the LUB2 code again prepares an IDP at a desired axial station by the necessary three-dimensional calculations. This method is somewhat tedious but can produce an accurate IDP even when the angle of attack is over 30 degrees. In the preparation of IDP for the test cases, the spherical nose tips of the bodies were considered to have neither spin nor mass transfer.

NUMERICAL SOLUTION

The equations are solved by implicit differencing in the y, ϕ -plane. The x derivatives are approximated by a backward difference while y and ϕ derivatives use an unequally spaced three-point difference formula, e.g.,

$$\frac{\partial f}{\partial x} = \frac{f_j - f_{j-1}}{\Delta x}$$

and

$$\frac{\partial f}{\partial y} = \alpha_{k-1} f_{k-1} + \alpha_k f_k + \alpha_{k+1} f_{k+1}$$

DTIC COPY PREPARED		Distribution For CH&I <input checked="" type="checkbox"/> T'B <input type="checkbox"/> Unpublished <input type="checkbox"/> Publication <input type="checkbox"/>
Distribution/ Availability Codes Avail and/or Special		A

where the α_i are determined from the Taylor series expansions of f_{k-1} and f_{k+1} around the k -th location, and hence they are functions of the stepsize between the grid points.

The PNS equations and the perturbation equations during the iterations can be written in the matrix form

$$\underline{F}(\underline{U}) = 0$$

$$\underline{\Delta}^n = \underline{U}^{n+1} - \underline{U}^n$$

where \underline{F} denotes the governing equations for the unknowns \underline{U} , and $\underline{\Delta}^n$ is the column matrix of perturbation properties at n -th iteration.

After differencing, the equations are linearized by the Newton-Raphson method. Thus, all the nonlinear terms of perturbation properties are dropped. This results in an equation of the form

$$\underline{M}(\underline{U}^n) \underline{\Delta}^n = -\underline{F}(\underline{U}^n) ; \quad n = 0, 1, 2, \dots$$

with \underline{U}^0 an initial guess to the solution of the governing equations, and \underline{M} the Jacobian of \underline{F} . Because of the size of the system, instead of solving the above equation directly, the Gauss-Seidel iteration method is used. In the ϕ -direction, an implicit-iterative scheme⁸ is used, but after convergence, the solution obtained is a fully implicit one. After convergence, another step in the marching direction is taken and the whole procedure is repeated.

Convergence problems often occur when the marching solution encounters a strongly separated region due to crossflow. To reduce the problem, either zero or explicit pressure gradient model may be used. Smaller marching step-sizes and/or pressure smoothing in the y coordinate direction also can help the convergence. When the angle of attack is very high, more careful selection of grid sizes and preparation of more accurate initial plane data are required in order to start a solution.

Mass transfer and spin add more disturbances in the viscous flowfield, thus deteriorating the convergence of the solution. A large mass-transfer distribution along the body can cause an axial flow separation at some downstream station which causes the marching solution to fail. To reduce the marching stepsize problem in a solution, the marching stepsizes are controlled internally by the code considering the number of iterations taken for the solution at the previous step.

RESULTS AND DISCUSSION

For the present study, a body-generator coordinate system is used with x along the body, y normal to the body and ϕ around the body, and it does not rotate with the body. Figure 1 shows the coordinate system and the sign conventions for aerodynamic coefficients. Since this sign convention is not a universal one, it is recommended to be used only for the interpretation of the directions of the forces and moments reported in this paper.

The initial plane data for the test cases have been obtained using a perfect gas viscous shock-layer approach (VSL) at the sphere-cone tangency point, and all the flow properties together with forces and moments are transferred to the PNS solution. To start the PNS solution, an initial marching step-size of less than one-tenth of the nose radius has been used, and it was increased internally in the code, considering the number of iterations taken and the maximum permissible marching stepsize for a meaningful solution. In the present calculations, 101 grid-points in the normal direction and 19 planes around the body are used for all cases.

The original PNS code utilized the continuity equation in order to predict the wall pressure at the body boundary when the body had mass transfer. However, by numerical experiment, it has been found that the method is likely to give an unstable and divergent solution even in the case of very small mass transfer. Therefore, in the present work the v-momentum equation is taken and differenced at the body boundary. By this method, stable solutions have been obtained in most cases with moderate mass transfer. A large mass transfer at the wall can cause an axial flow separation at some downstream station. In such a case, it should be noted that the PNS method cannot treat the primary flow separated region.

In the case of high angle of attack with large mass transfer and spin, a relatively large amount of perturbations can occur in the viscous flowfield. These perturbations have an adverse effect on the convergence of a solution. For this reason, in the present computations, the zero pressure gradient model in the marching direction was used to improve the convergence. The effect of the three different kinds of axial pressure gradient models has been discussed in detail by Waskiewicz and Lewis.⁷

To investigate the effect of mass transfer and/or spin on the viscous flow past a sphere-cone geometry, two sets of freestream conditions have been chosen and parametric computations have been made. Case 1 considers a freestream condition of $M = 5$, $\alpha = 2$ and $Re_\infty/ft = 6.21 \times 10^5$. Case 2 considers a freestream condition of $M = 18$, $\alpha = 15$ and $Re_\infty/ft = 5.45 \times 10^5$. The body geometry is a spherically blunted 7-deg half-angle cone 0.817 ft long. For both cases, a parametric comparison is presented to study the effect of spin, the effect of mass transfer, and the coupling effect of mass transfer and spin. For Case 1, the effect of the asymmetric mass-transfer distribution around the body as well as constant mass-transfer distribution will be analyzed in detail. Spin rates considered are 2000 and 8000 rev/min. Case 1a has a sinusoidal mass-transfer distribution around the body, and the maximum value of mass-transfer rate is 0.0025. Case 1b and Case 2 have a mass transfer rate of 0.00125, which is constant along and around the body. Details of the freestream conditions are given in Table 1.

For Case 1, the flowfield solution over the body with mass transfer could not be obtained up to the body end. For Case 1a with mass transfer only, the solution was obtained up to $s = 24.8$ where axial flow separation occurred due to the mass-transfer effect. For Case 1a with both mass transfer and spin, the solution was obtained up to $s = 23.3$ before axial flow separation occurred. The effect of mass transfer on axial flow separation will be further discussed later.

Figure 2 shows a sinusoidal distribution of mass transfer for Case 1a, which is designed to exert a relatively large side force in the minus direction. In Figure 3, the Magnus force due to the sinusoidal mass-transfer distribution is shown, and also it can be observed that the coupling effect of mass transfer and spin on the Magnus force is remarkable. Figure 4 shows the Magnus force components distribution along the body for Case 1a, where it is noted that the Magnus force component due to the wall pressure distribution constitutes the largest part of the total Magnus force, while the components due to the axial and the circumferential shear stresses are negligible.

For Case 1b, we have constant mass transfer around the body. Hence in this case, the Magnus force due to mass transfer should be negligible. In Figure 5, it is noted that the Magnus force due to the coupling effect of the mass transfer and spin is substantial, and the effect is over three times as much as the spin-only effect on the Magnus force. The Magnus force component due to the wall pressure prevails over the others due to the wall shear stresses for this case as shown in Figure 6.

Figure 7 shows the effect of mass transfer and spin on the Magnus force for Case 2 which has relatively large Mach number and high angle of attack. For this case, it is noted that the coupling effect of mass transfer and spin is again remarkable. Therefore, on the basis of the present computational results, it is concluded that this coupling effect should not be neglected in a flight dynamics analysis of slow-spin reentry vehicle with mass transfer. Figure 8 shows that the Magnus force component due to the crossflow shear stress is not negligible, and it has a different direction from the F_{p_w} for the Case 2.

The effect of mass transfer and spin on the wall pressure is shown in Figure 9, where the spin effect was almost negligible. Hence, the differences shown are largely due to mass transfer. It is noted that the mass-transfer effect increases the wall pressure because the thickening of the viscous layer increases the displacement-induced pressure interaction. In this figure, an unstable solution due to axial flow separation can be seen at $s = 24$ and $\phi = 180$ deg.

Figure 10 shows the effect of asymmetric mass transfer and spin on the wall pressure at $s = 23$. In fact, the pressure difference between the two cases is due mostly to the mass-transfer effect. Since Case 1a has maximum mass transfer in the $\phi = 270$ -deg plane of the body, the pressure difference is larger on this plane of the body, as can be seen in the figure. Figure 11 shows the effect of mass transfer and spin on the shock-layer thickness which slightly increases the shock-layer thickness. Figure 12 shows the effect of mass transfer and spin on the shock-layer thickness around the body at $s = 23$ where the slight increase in the shock-layer thickness is due mostly to the mass transfer effect, not the spin effect.

The effect of mass transfer and spin on the surface heat transfer along the body is shown in Figure 13. Mass-transfer effect decreases the wall heat transfer, and the effect is more sizable on the windward side. Figure 14 shows the effect of asymmetric mass transfer and spin on the heat transfer at $s = 23$ for Case 1a. The big asymmetric difference between the two cases is largely due to the mass-transfer effect. Figures 15 and 16 show the effects

of mass transfer and spin on the streamwise wall shear, and the effects are quite similar to the effects on the heat transfer. Figure 17 shows the effects of asymmetric mass transfer and spin on the crossflow wall shear at $s = 23$. The effect is to decrease the shear stress in absolute value on both sides of the body. As previously mentioned, for Case 1 the spin effects on wall pressure, shock-layer thickness, heat transfer, and wall shear were very small compared to the mass-transfer effects. However, for Case 2 which has a larger spin rate than Case 1, the spin effect was not negligible, which will be shown later.

Figure 18 shows the effect of mass transfer on axial flow separation for Case 1a. In the figure it can be observed that the mass transfer retards the axial flow velocity in the boundary layer. The effect becomes larger further downstream, and finally the axial flow separates at $s = 24$ as can be seen in the figure. The PNS method cannot treat the axial-flow separated region, hence the solution diverged at this station. In the downstream region before axial flow separation, the numerical solution took a relatively large number of iterations and small marching stepsizes. This effect resulted in the relatively large computing time for this case as can be seen in Table 3.

Case 2 had a spin rate of 8000 rpm and constant mass-transfer rate of 0.00125. The computational results for this case showed more sizable effects of spin on the wall pressure and other surface properties. Hence, parametric comparisons will be presented for this case. Figures 19 and 20 show the wall pressure in case of mass transfer and spin. Actually it was hard to distinguish each effect separately in this kind of figure. Hence, it was desirable to compare the ratios of each pressure to its basic value. Here, the basic value means the computed wall pressure for the body with neither mass transfer nor spin. Thus, Figure 21 shows the coupling effect as well as the separate effects of mass transfer and/or spin on the wall pressure. In this figure, the spin effect appears antisymmetric, while the mass-transfer effect is symmetric around the body. The coupling effect is quite clear, and it has nearly additive characteristic. The spin effect decreases the surface pressure in $\phi = 0 - 180$ -deg of the body, and increases the pressure in $\phi = 180 - 360$ -deg of the body, thus producing a negative Magnus force as can be expected. The symmetric mass transfer itself cannot produce a Magnus force, but it increases the wall pressure symmetrically. From Figures 20 and 21 it is observed that at station $s = 30.06$ a strongly separated flow is developed in the crossflow direction. For this case at $\alpha = 15$ -deg, the crossflow separation begins as early as $s = 6$, as can be seen in Figures 32 and 33.

Figures 22 and 23 show the shock-layer thicknesses along and around the body respectively where the effects of mass transfer and spin on the shock-layer thickness appear negligible. Figure 24 shows the effect of mass transfer and spin on the heat transfer in the windward and leeward planes. A parametric comparison of the effect of mass transfer and/or spin on the heat transfer around the body at $s = 30.06$ is presented in Figure 26, and it can be interpreted on the basis of the data given in Figure 25. The spin effect on the heat transfer around the body turns out quite complex due to the crossflow separation as shown in Figure 26. The mass-transfer effect is symmetric and decreases the wall heat transfer. The coupling effect is approximately additive of both effects. Figures 27 - 29 show the effects of mass transfer and/or spin on the streamwise wall shear, and the effects have similar trends to the effects on the heat transfer.

Figures 30 and 31 show the effects of mass transfer and/or spin on the crossflow wall shear around the body at $s = 30.06$. The effects frequently change their directions due to crossflow separation. The coupling effect is again additive of both effects. Since the current PNS method is elliptic in the crossflow direction, it can solve the crossflow separated region. But the crossflow separation produces more perturbations in the flowfield, and the perturbations have an adverse effect on the convergence of a solution. Therefore, generally smaller marching stepsizes are required to pass through the region where the crossflow separation begins. Mass transfer causes crossflow separation at an earlier station on the body while spin suppresses the crossflow separation. A definition of crossflow separation in the case of spinning body has been introduced by Agarwal and Rakich.¹⁰ The criterion generalizes the Moore-Rott-Sears criterion for two-dimensional unsteady separation. The onset of separation in the flowfield is characterized by the condition $\partial w / \partial y = 0$ at $w = 0$ where w is the circumferential component of velocity and y is the coordinate normal to the body.

Figure 32 shows the effect of spin on crossflow separation at $s = 6.4$ and $\phi = 160$ -deg for Case 2. The basic case already has the separated crossflow profile at this station. But for the spin case, the profile is not separated yet at this station due to the definition introduced above. Figure 33 shows the effect of mass transfer on crossflow separation. It is observed that mass transfer causes crossflow separation at an earlier station on the body. As previously mentioned, mass transfer can cause axial flow separation also. In a numerical experiment, mass transfer of a few percent of $\rho_{\infty} U_{\infty}$ was found to easily cause an axial flow separation within a few nose radii downstream. In the case of low mass transfer as in Case 1a, the axial flow was separated at $s = 24$.

Table 2 summarizes all the force and moment coefficients obtained from the parametric computations for the two test cases. The effect of the spin on the axial and normal forces is found to be negligible while the effect on the Magnus side force is sizable. An asymmetric mass transfer also can produce a finite amount of side force. From the table, it is also observed that the mass transfer decreases the normal and axial forces. An important fact found in the present work is that mass transfer and spin have a measurable coupling effect on the Magnus side force, which is shown in Table 2 as well as in the figures. However, no experimental data are known to the authors at this time to validate the present results for the coupling effects.

Computing times for these cases are given in Table 3. These times were obtained on the IBM 3032 system at Virginia Polytechnic Institute and State University. Most cases consumed less than 40 minutes of CPU time for the entire solution, but the solutions for Case 1a and 1b with mass transfer took relatively longer computing times because of the small stepsizes taken before axial flow separation.

SUMMARY

The viscous flowfield over a sphere-cone undergoing mass transfer and/or spin at angle of attack has been calculated using the parabolized Navier-Stokes equations. In the mass-transfer case, the wall pressure is obtained using the v -momentum equation rather than continuity equation to facilitate

the convergence. The main results of the present work can be summarized as follows:

1. The coupling effect of mass transfer and spin on the Magnus force is remarkable, i.e., it is much more than the additive effect.
2. Mass transfer has a tendency to reduce the axial and normal forces, and it increases the wall pressure and decreases the heat transfer and wall shear stresses.
3. Mass transfer causes earlier axial and crossflow separations.
4. Spinning motion has negligibly small effect on the normal and axial forces, and it produces asymmetric effects on the wall pressure as well as the other surface properties around the body.
5. Spin has a tendency to suppress the appearance of crossflow separation at high angles of attack.

REFERENCES

1. Murray, A. L. and Lewis, C. H.: "Hypersonic Three-Dimensional Viscous Shock-Layer Flows over Blunt Bodies," AIAA J., Vol. 16, No. 12, December 1978, pp. 1279-1286.
2. Murray, A. L. and Lewis, C. H.: "Heat and Mass-Transfer Effects on Three-Dimensional Viscous Shock-Layer Flows," AIAA Paper 78-844, May 1978.
3. Whitehead, R. E. and Davis, R. T.: "Numerical Solutions to the Viscous Shock-Layer Blunt Body Problem with Inert Gas Injection," Sandia Laboratories, SC-CR-70-6162, January 1971.
4. Lubard, S. C. and Helliwell, W. S.: "Calculation of the Flow on a Cone at High Angle of Attack," AIAA J., Vol. 12, No. 7, July 1974, pp. 965-974.
5. Waskiewicz, J. D. and Lewis, C. H.: "Hypersonic Viscous Flows over Sphere-Cones at High Angles of Attack," AIAA Paper 78-64, AIAA 16th Aerospace Sciences Meeting, Huntsville, AL, January 1978.
6. Gogineni, P. R. and Lewis, C. H.: "Three-Dimensional Viscous Hypersonic Flows over General Bodies," AIAA Paper 80-0029, AIAA 18th Aerospace Sciences Meeting, Pasadena, CA, January 1980.
7. Agopian, K., Collins, J., Helliwell, W. S., Lubard, S.C., and Swan, J.: "NASA Viscous 3-D Flowfield Calculations," R&D Associates, RDA-TR-6100-007, October 1975.
8. Helliwell, W. S., Dickinson, R. P., and Lubard, S. C.: "HYTAC Phase I Report: Viscous Flow over Arbitrary Geometries at High Angle of Attack," Arete Associates Technical Report, AR-79-046-TR, April 24, 1979.

9. Kim, M. D., Thareja, R. R., and Lewis, C. H.: "Three-Dimensional Viscous Flowfield Computations in a Streamline Coordinate System," AIAA Paper 81-0401, AIAA 19th Aerospace Sciences Meeting, St. Louis, MO, January 1981.
10. Agarwal, R. and Rakich, J. V.: "Computation of Hypersonic Laminar Viscous Flow Past Spinning Sharp and Blunt Cones at High Angle of Attack," AIAA Paper 78-65, January 1978.
11. Agarwal, R. and Rakich, J. V.: "Computation of Supersonic Laminar Viscous Flow Past a Pointed Cone at Angle of Attack in Spinning and Coning Motion," AIAA Paper 78-1211, July 1978.
12. Sturek, W. B. and Schiff, L. B.: "Computations of the Magnus Effect for Slender Bodies in Supersonic Flow," AIAA Paper 80-1586, 1980.

NOMENCLATURE

c_p	constant pressure specific heat
CFS	streamwise skin-friction coefficient, $2\tau_x^*/(\rho_\infty U_\infty^2)$
CFW	crossflow skin-friction coefficient, $2\tau_\phi^*/(\rho_\infty U_\infty^2)$
C_A	axial force coefficient
C_N	normal force coefficient
C_Y	Magnus force coefficient
C_m	pitching moment coefficient about blunt nose-tip
C_n	Magnus moment coefficient about blunt nose-tip
F_{τ_x}	$\sin^2 \theta_c \int_0^x \int_0^{2\pi} x \sin \phi \tau_x(x, \phi) d\phi dx$
F_{p_w}	$\frac{1}{2} \sin 2\theta_c \int_0^x \int_0^{2\pi} x \sin \phi p_w(x, \phi) d\phi dx$
F_{τ_ϕ}	$\sin \theta_c \int_0^x \int_0^{2\pi} x \cos \phi \tau_\phi(x, \phi) d\phi dx$
FY	total Magnus side force, $F_{\tau_x} + F_{p_w} + F_{\tau_\phi}$
H	total enthalpy, H^*/U_∞^2
h	static enthalpy, $h^*/(C_p^* T_\infty)$
L	reference length, equivalent cone slantwise length
M	freestream Mach number

\dot{m}	mass-transfer rate at wall, $\rho_w^* v_w^* / \rho_\infty U_\infty$
p	nondimensional pressure, $p^* / (\rho_\infty U_\infty^2)$
p_w	wall pressure, $p_w^* / \rho_\infty U_\infty^2$
Pr	Prandtl number
q	heat-transfer rate, $q^* / (\rho_\infty U_\infty^3)$
r	local body radius, r^* / L
R_n	dimensional body nose radius of curvature
Re_∞ / ft	freestream unit Reynolds number
STINF	Stanton number, $q^* / [\rho_\infty U_\infty (H_0^* - H_w^*)]$
s	surface distance coordinate measured along the body from nose tip, s^* / R_n
T	temperature, T^* / T_∞
T_0	freestream stagnation temperature
T_{ref}	reference temperature, $(\gamma - 1) M^2 T_\infty$ or U_∞^2 / C_p^*
T_w	wall temperature, T_w^* / T_∞
U_∞	dimensional freestream velocity
u	velocity in the x direction, u^* / U_∞
v	velocity in the y direction, v^* / U_∞
w	velocity in the ϕ direction, w^* / U_∞
x	coordinate along the body surface with constant ϕ , x^* / L
y	coordinate normal to the surface, y^* / L
YSH	bow-shock standoff distance divided by R_n
Z_{cp}	center of pressure from blunt nosetip in percentage of the blunt body axial length
α	angle of attack, degree
γ	ratio of specific heats
η	transformed normal coordinate, y / ξ

ϵ	perturbation parameter, $\epsilon^2 = \mu^* (T_{ref}) / (\rho_\infty U_\infty R_n)$
θ_c	cone half-angle, degree
μ	coefficient of viscosity, μ^* / μ_∞
ξ	bow-shock standoff distance divided by L
ρ	density, ρ^* / ρ_∞
τ_x	primary flow wall shear stress, $\tau_x^* / (\rho_\infty U_\infty^2)$
τ_ϕ	crossflow wall shear stress, $\tau_\phi^* / (\rho_\infty U_\infty^2)$
ϕ	circumferential coordinate
Ω	angular velocity (rev/min)

Subscript

w	wall value
0	stagnation condition
∞	freestream condition (dimensional quantity)

Superscript

*	dimensional quantity
---	----------------------

TABLE 1
Test Case Freestream Conditions and Body Geometries

Case	S U_{∞} (fps)	M T_{∞} ($^{\circ}$ R)	Re_{∞} (1/ft) α (deg)	R_n (ft) θ_c (deg)	T_w ($^{\circ}$ R) T_w/T_0	ϵ	Ω (rpm)	\dot{m} (max)
1a	30.06 2341.	5. 91.247	621000. 2.	0.027917 7.	460. 0.84	0.0218	2000.	0.00250 dist.
1b	30.06 2341.	5. 91.247	621000. 2.	0.027917 7.	460. 0.84	0.0218	2000.	0.00125 const.
2	30.06 7223.	18. 64.80	544740. 15.	0.027917 7.	540. 0.1266	0.0545	8000.	0.00125 const.

Dist.: asymmetric distribution around body and constant along body.
Const.: constant around and along body.

TABLE 2
Aerodynamic Coefficients for Test Cases

Case	\dot{m} (max)	Ω (rpm)	C_A	C_N	C_Y	C_m	C_n	Z_{cp}
1a basic	0.0	0.0	0.1880	0.0372	-0.0	-0.0214	0.0	0.577
1a Ω only	0.0	2000.	0.1880	0.0372	-0.1850E-3	-0.0214	0.1280E-3	0.577
1a \dot{m} only	0.00250 dist.	0.0	0.1849	0.0285	-0.8471E-2	-0.0148	0.4902E-2	0.520
1a $\Omega + \dot{m}$	0.00250 dist.	2000.	0.1849	0.0284	-0.9392E-2	-0.0147	0.5609E-2	0.517
1b $\Omega + \dot{m}$	0.00125 const.	2000.	0.1840	0.0307	-0.5940E-3	-0.0166	0.4560E-3	0.538
2 basic	0.0	0.0	0.2070	0.4740	-0.0	-0.3075	0.0	0.649
2 Ω only	0.0	8000.	0.2070	0.4740	-0.5285E-3	-0.3075	0.3388E-3	0.649
2 \dot{m} only	0.00125 const.	0.0	0.2005	0.4703	-0.0	-0.3050	0.0	0.648
2 $\Omega + \dot{m}$	0.00125 const.	8000.	0.2005	0.4703	-0.8246E-3	-0.3050	0.5396E-3	0.648

Case 1a, case 1b: integrated up to $s = 23$.
Case 2: integrated up to $s = 30.06$
Reference area: body base area
Reference length: blunt body axial length
Moment: about blunt nosetip
 Z_{cp} : percentage of the blunt body axial length

TABLE 3

Computing Times* for Test Cases

Case	s	s-steps	grid size of n-points	ϕ -planes	time(min)
1a, basic	30.06	45	101	19	37.
1a, Ω only	30.06	45	101	19	37.
1a, \dot{m} only	24.80	82	101	19	73.
1a, $\dot{m} + \Omega$	23.33	70	101	19	65.
1b, $\dot{m} + \Omega$	30.06	58	101	19	54.
2, basic	30.06	45	101	19	38.
2, Ω only	30.06	45	101	19	38.
2, \dot{m} only	30.06	45	101	19	40.
2, $\dot{m} + \Omega$	30.06	45	101	19	40.

*CPU time on IBM 3032, H=OPT2 compiler

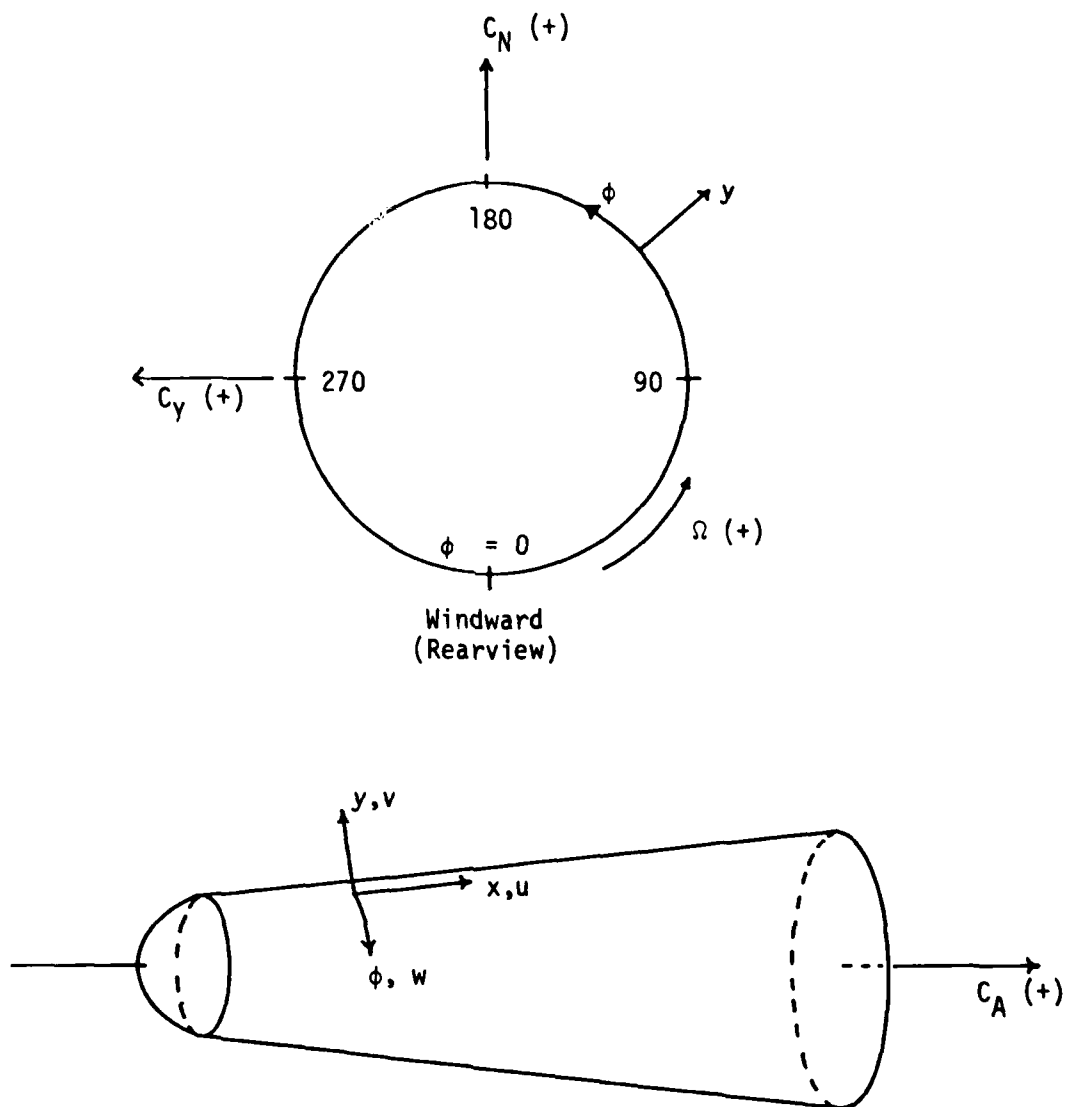


Figure 1. Body-generator coordinate system

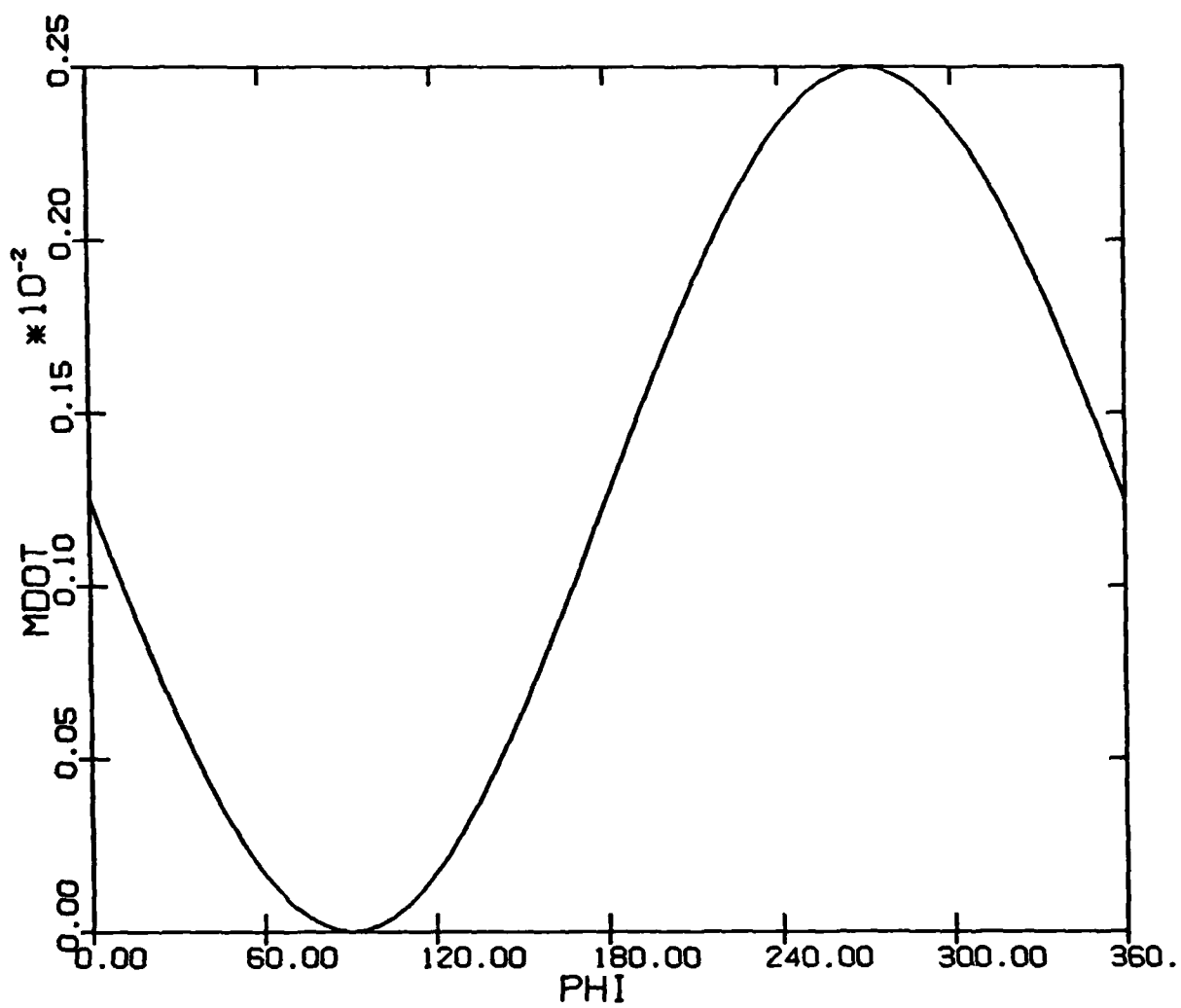


Figure 2: Case 1a Asymmetric mass-transfer distribution around the body.

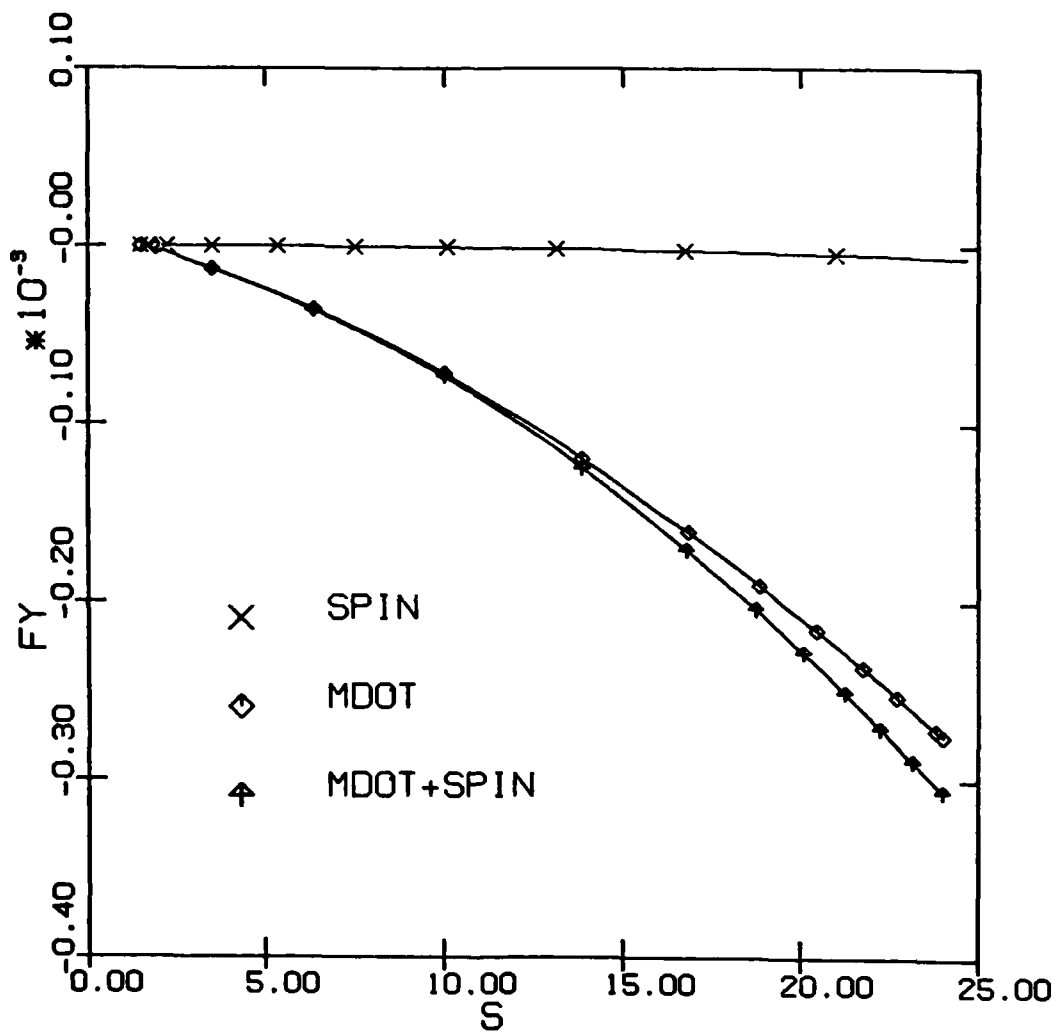


Figure 3: Case 1a Effects of asymmetric mass transfer and spin on the Magnus force along the body.

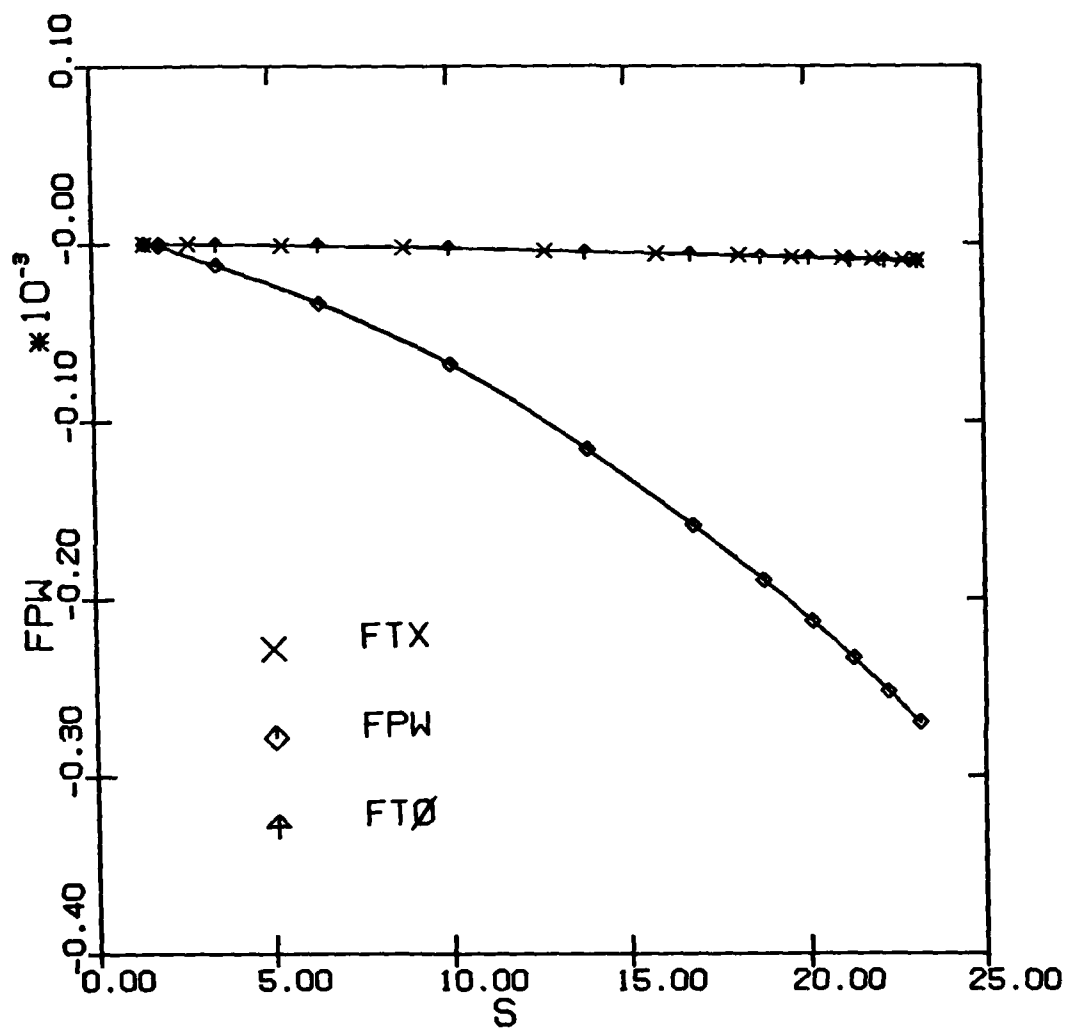


Figure 4: Case 1a Magnus force components along the body with mass transfer and spin.

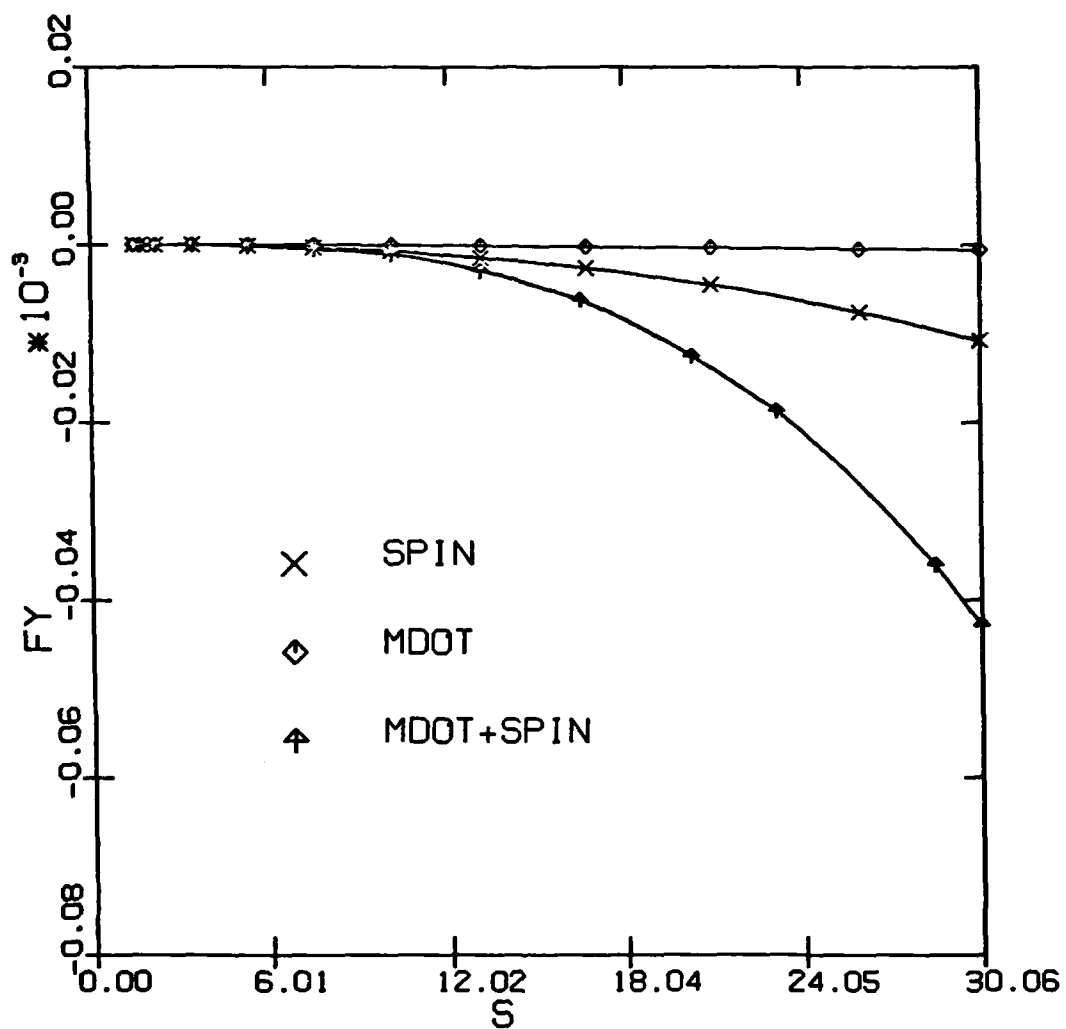


Figure 5: Case 1b Effects of constant mass transfer and spin on the Magnus force along the body.

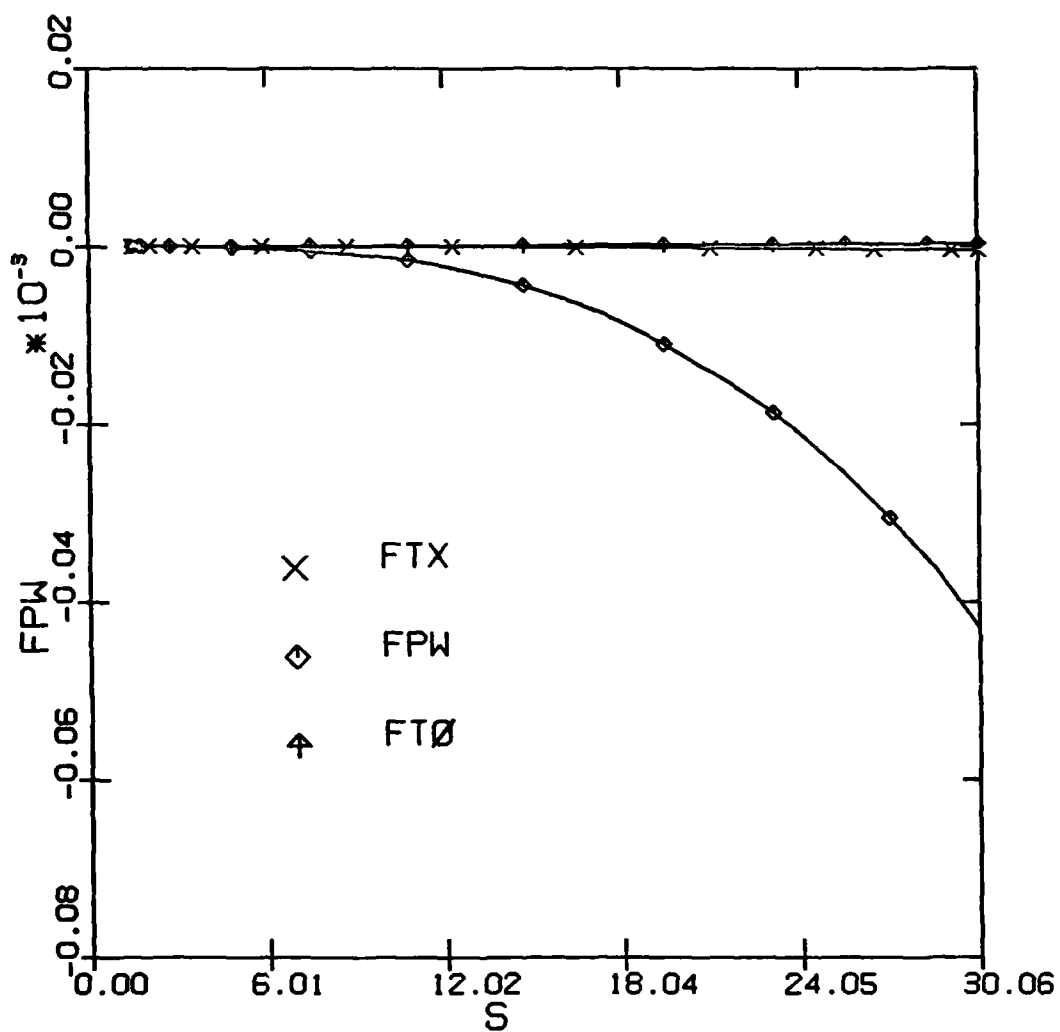


Figure 6: Case 1b Magnus force components along the body with mass transfer and spin.

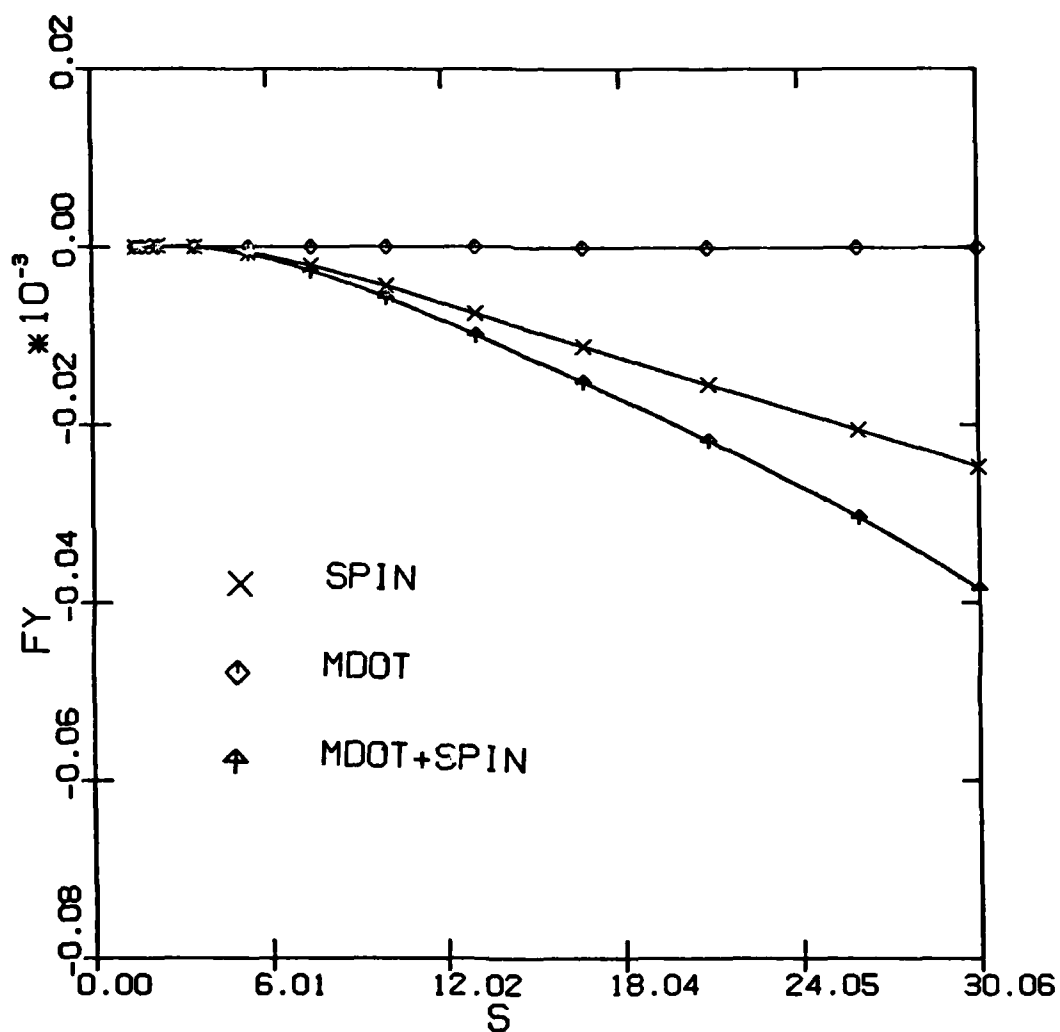


Figure 7: Case 2 Effects of constant mass transfer and spin on the Magnus force along the body.

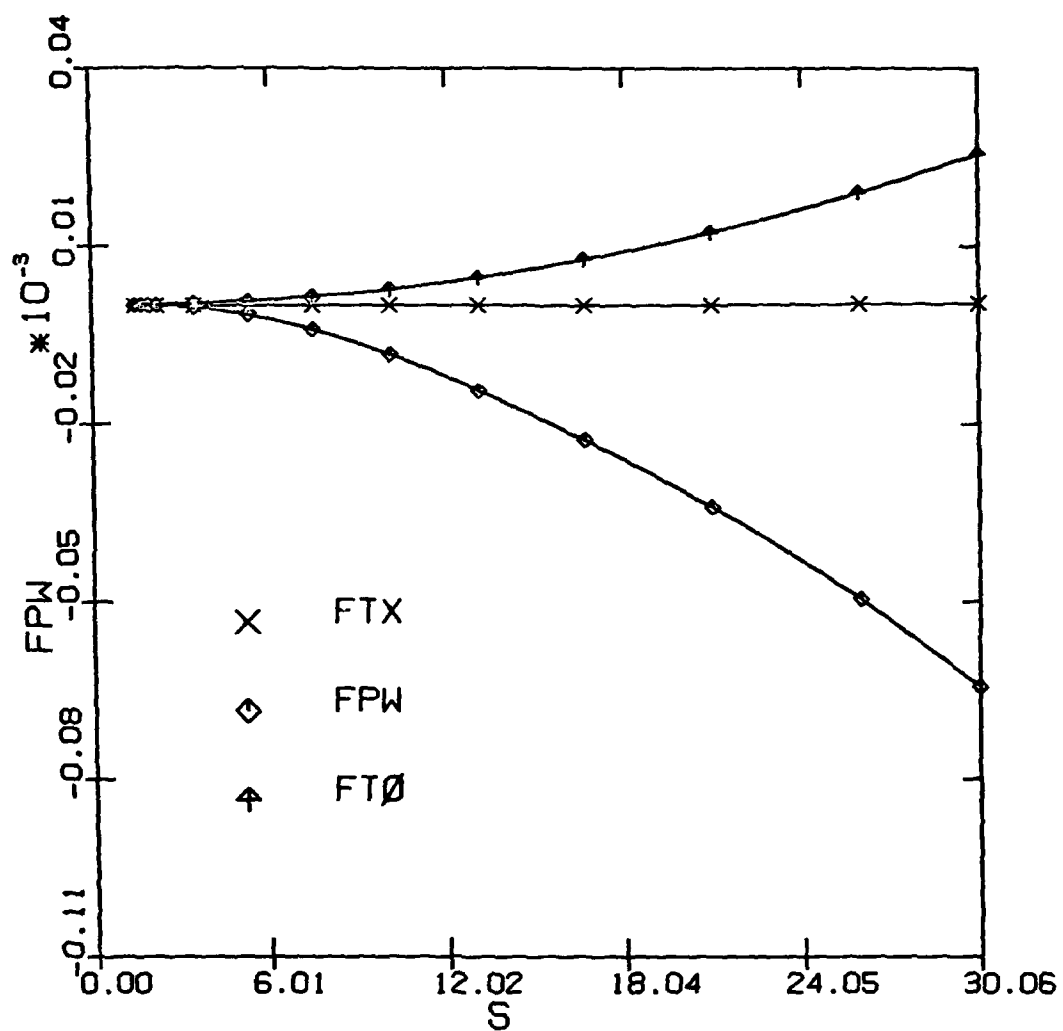


Figure 8: Case 2 Magnus force components along the body with mass transfer and spin.

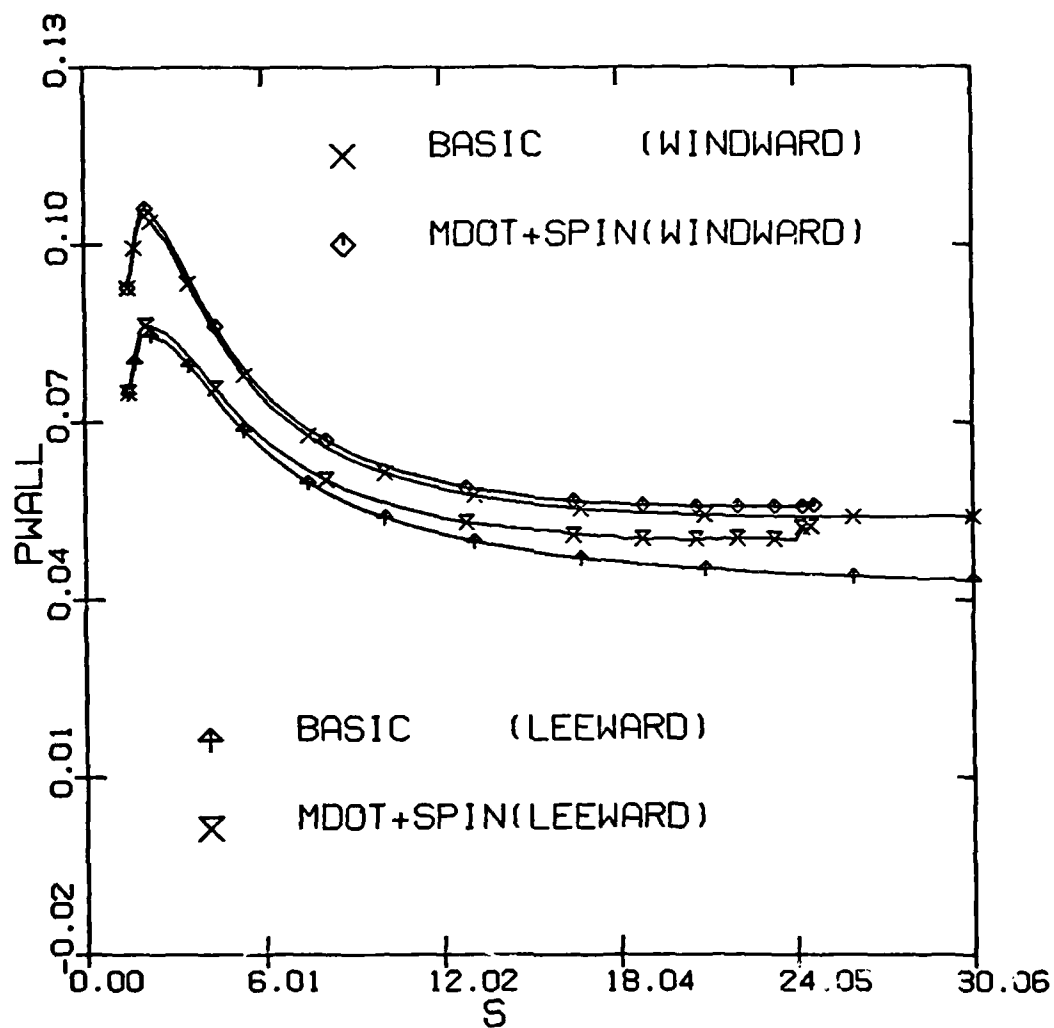


Figure 9: Case 1a Effects of mass transfer and spin on the surface pressure along the body.

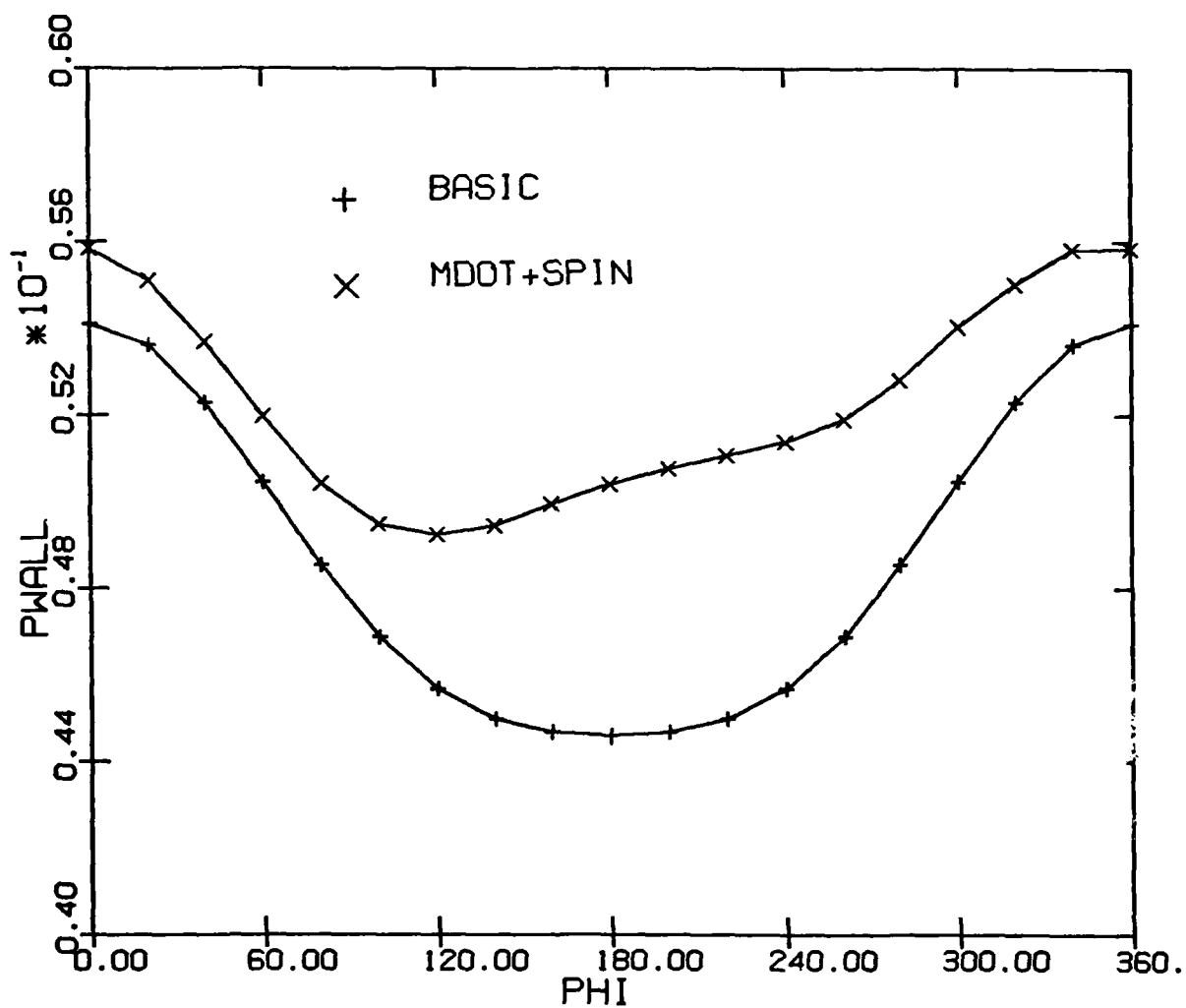


Figure 10: Case 1a Effects of asymmetric mass transfer and spin on the surface pressure around the body at $s = 23$.

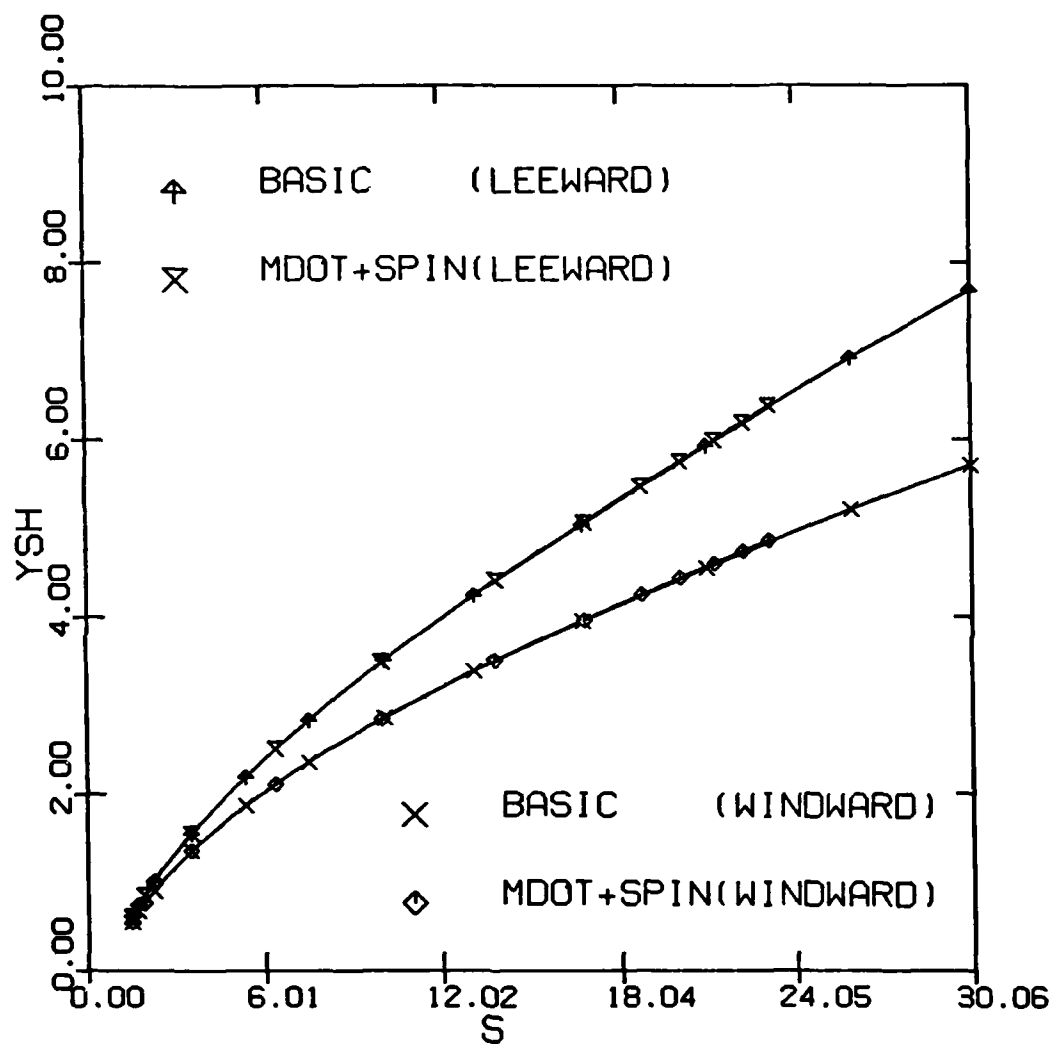


Figure 11: Case 1a Effects of mass transfer and spin on the shock-layer thickness along the body.

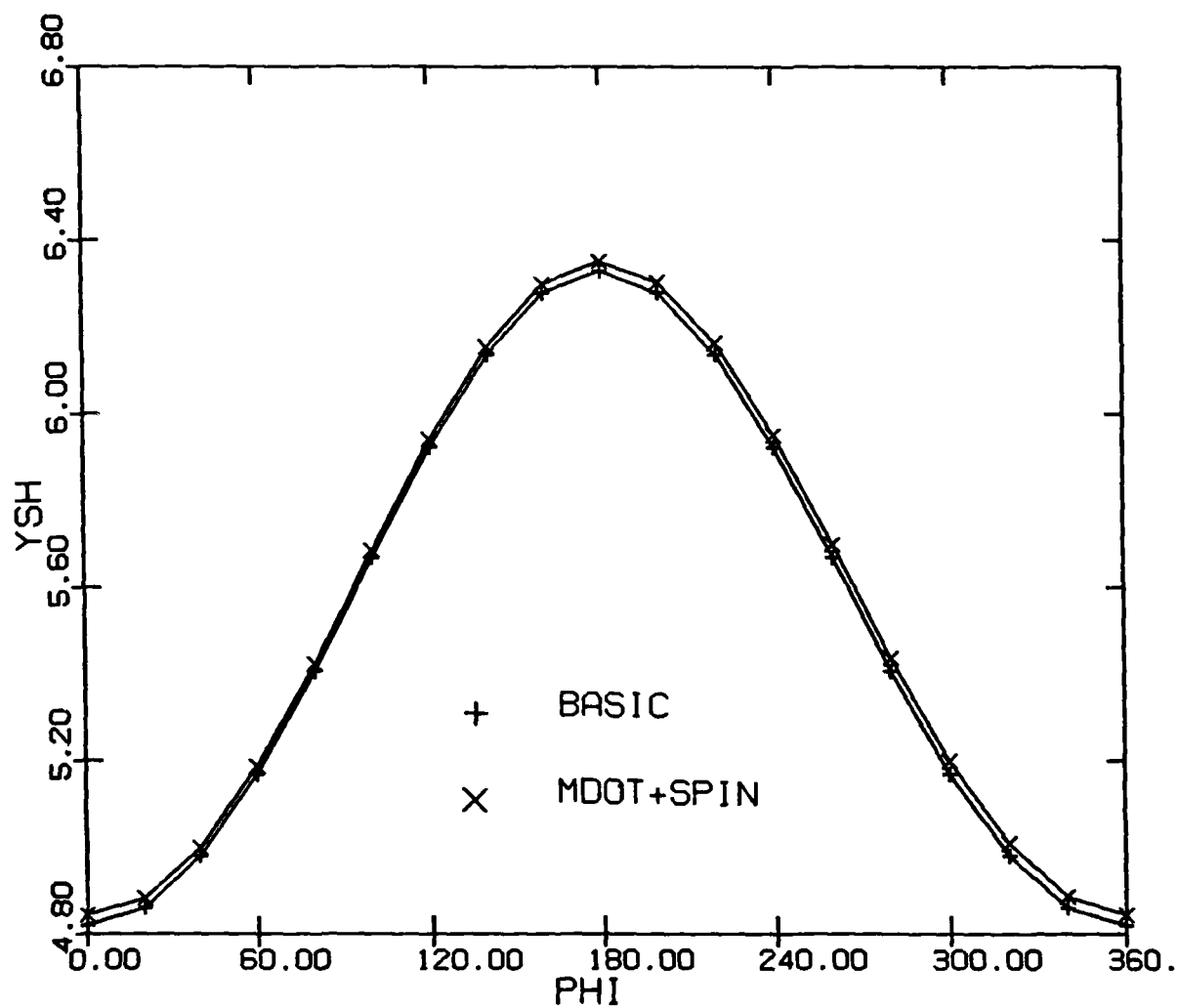


Figure 12: Case 1a Effects of asymmetric mass transfer and spin on the shock-layer thickness around the body at $s = 23$.

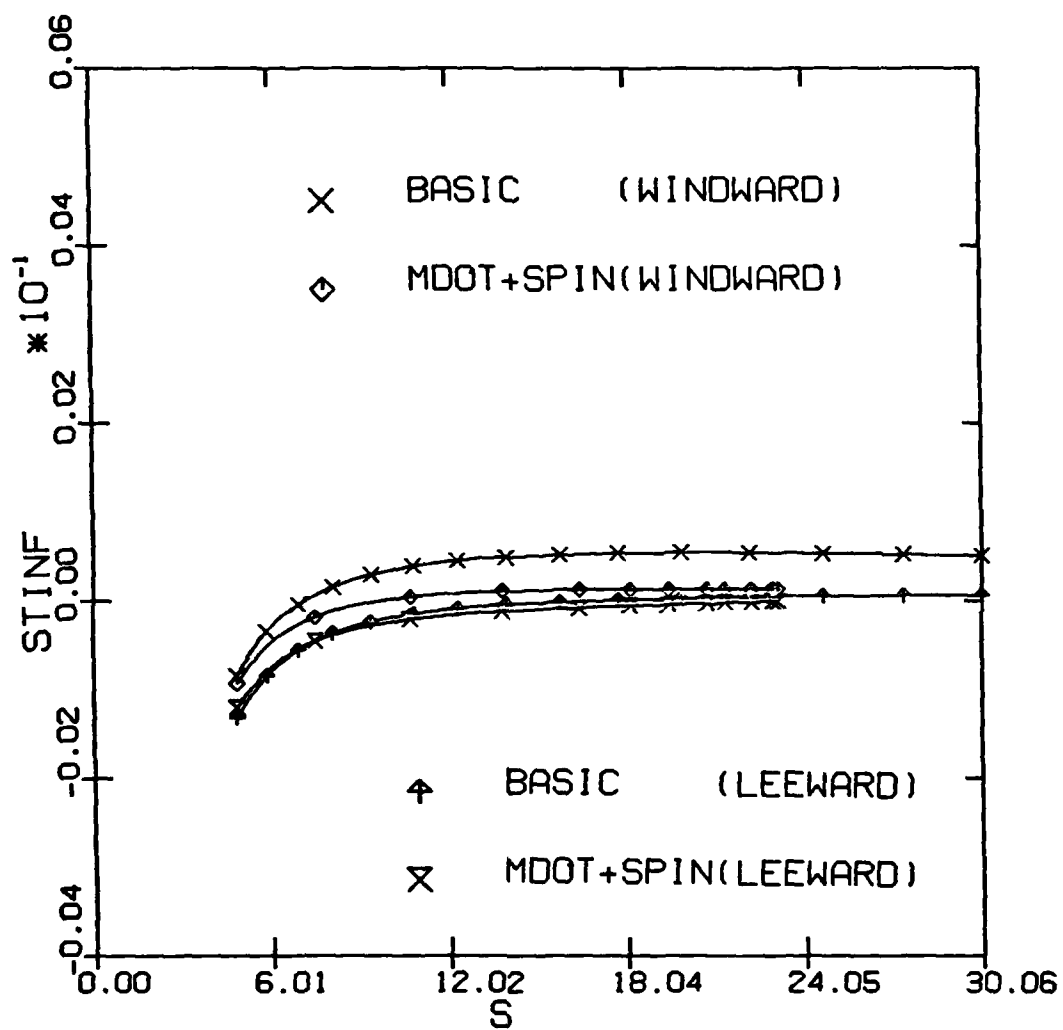


Figure 13: Case 1a Effects of mass transfer and spin on the heat transfer along the body.

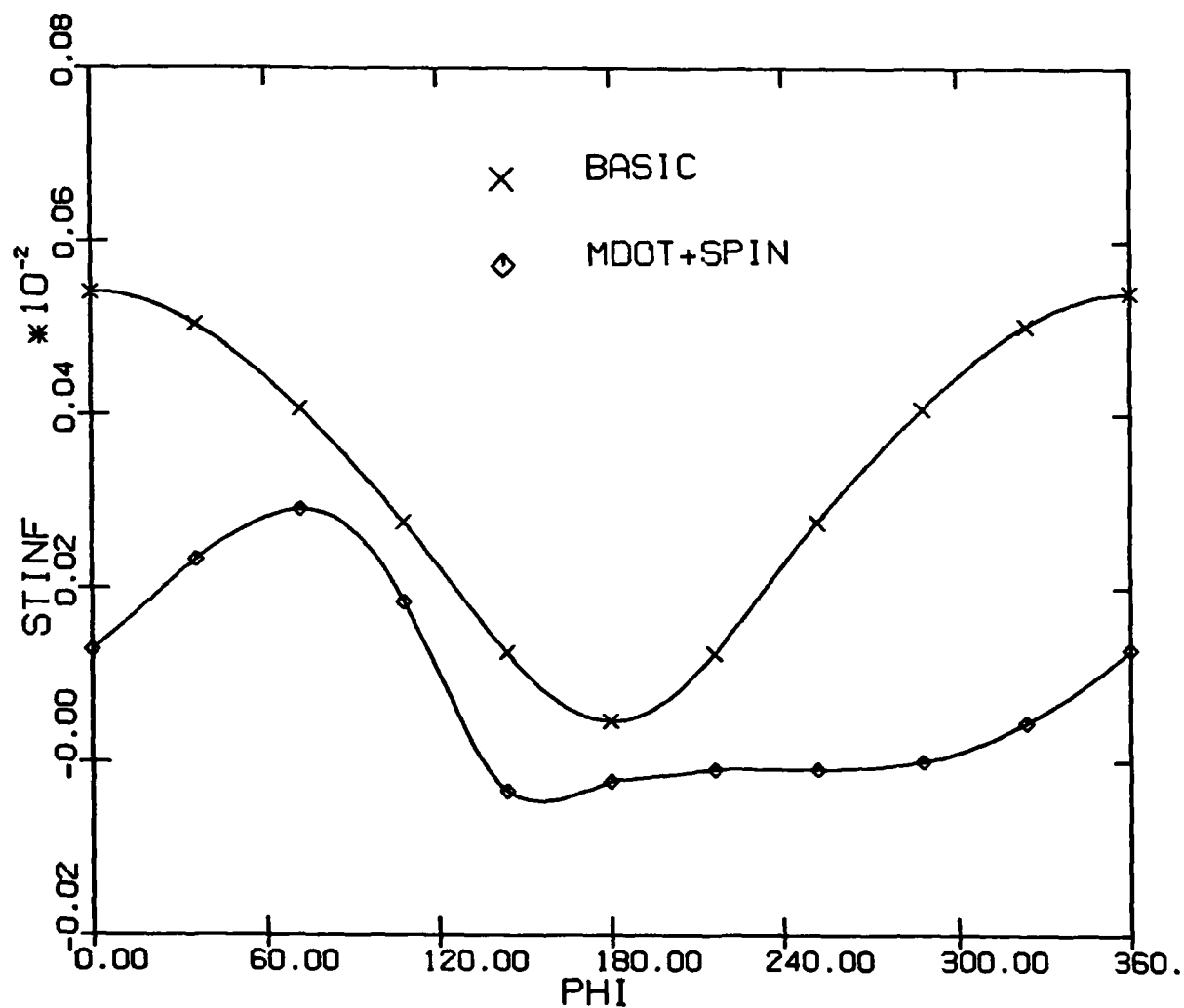


Figure 14: Case 1a Effects of asymmetric mass transfer and spin on the heat transfer around the body at $s = 23$.

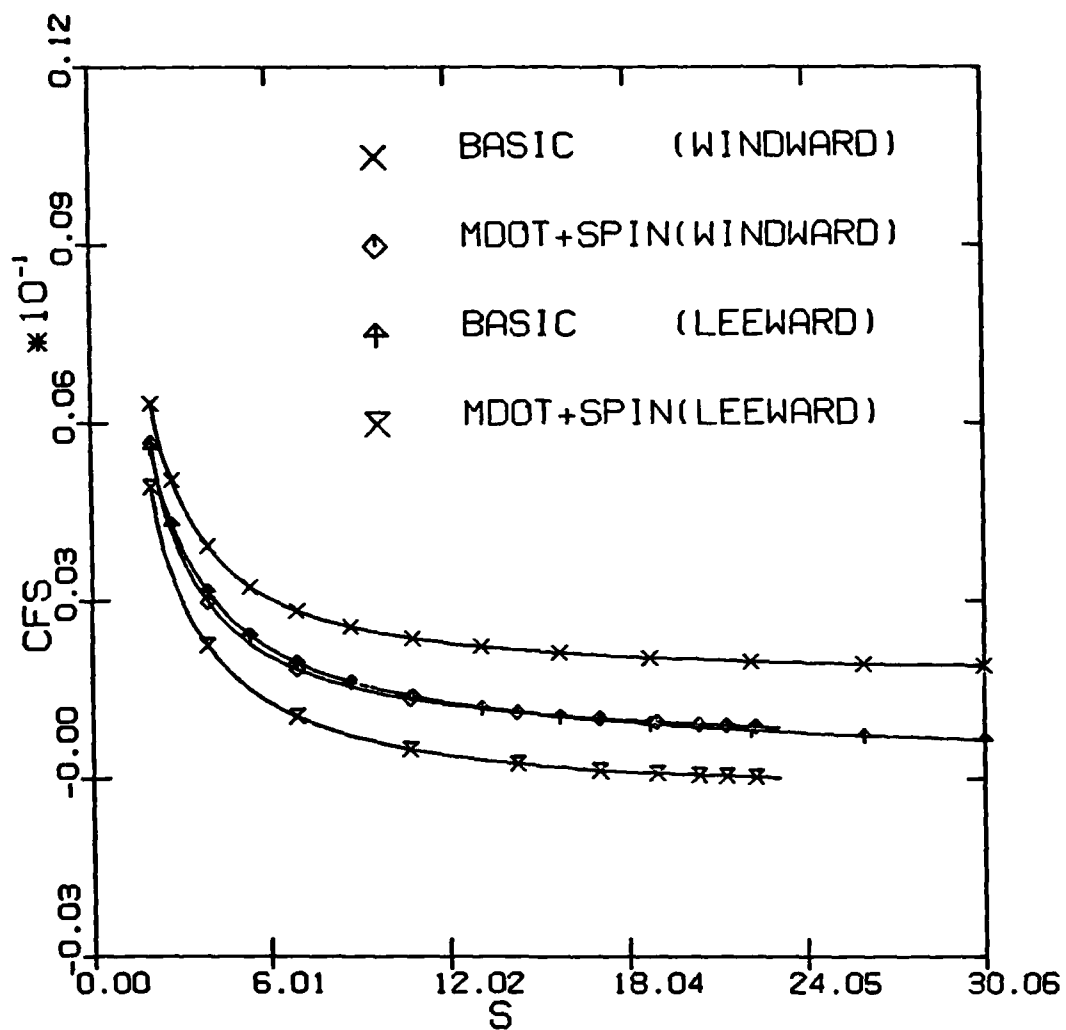


Figure 15: Case 1a Effects of mass transfer and spin on the streamwise shear along the body.

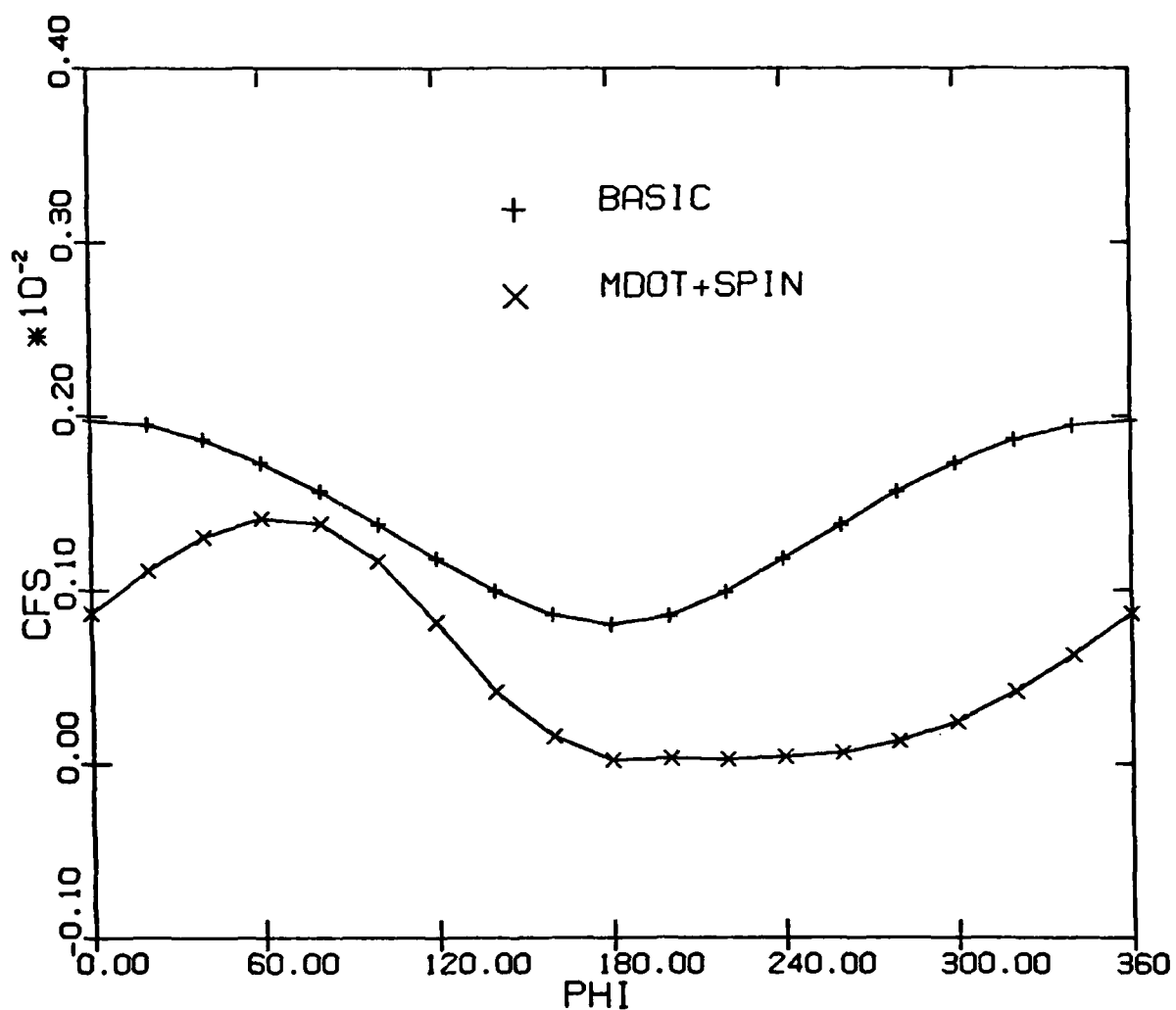


Figure 16: Case 1a Effects of asymmetric mass transfer and spin on the streamwise shear around the body at $s = 23$.

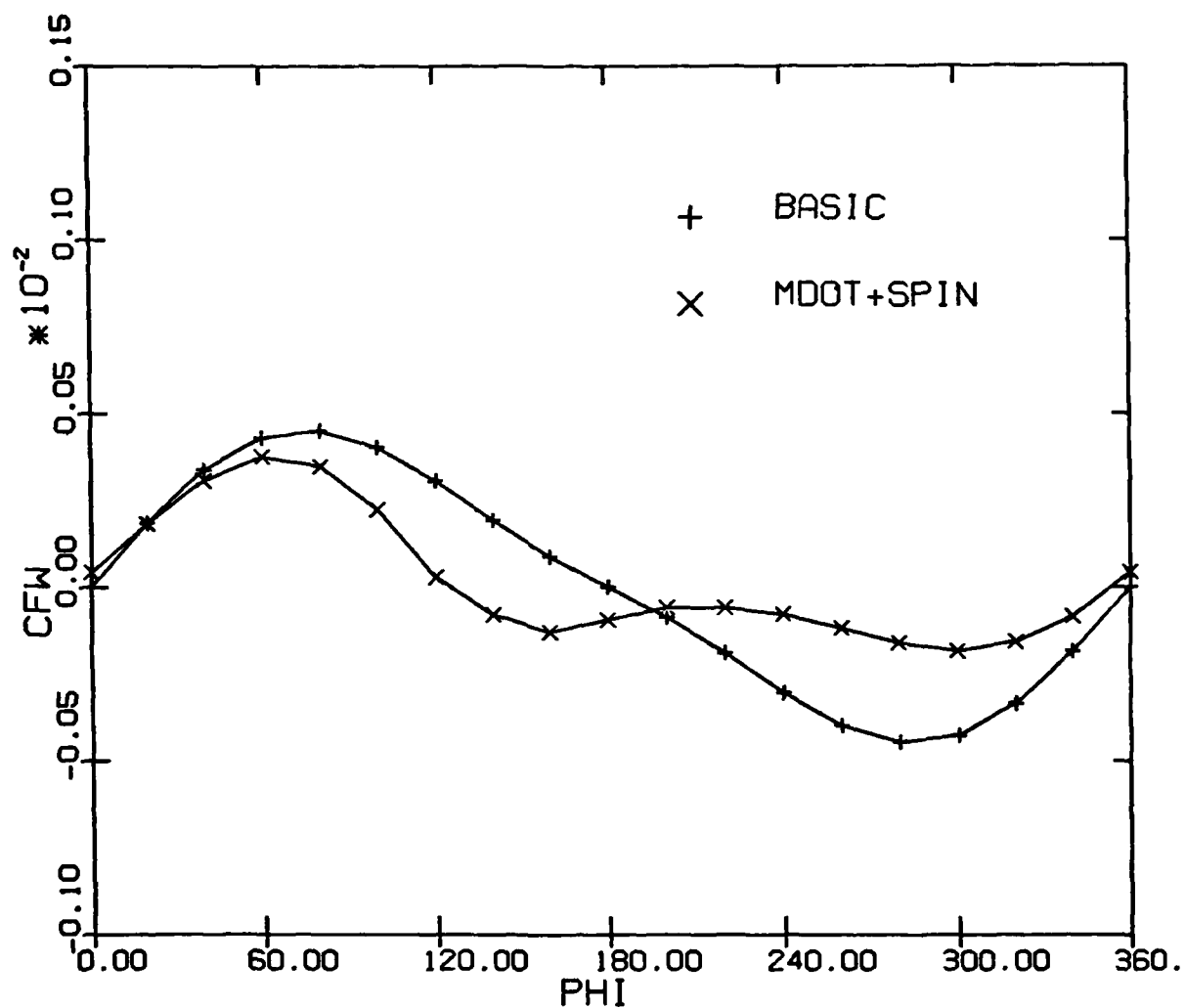


Figure 17: Case 1a Effects of asymmetric mass transfer and spin on the crossflow shear around the body at $s = 23$.

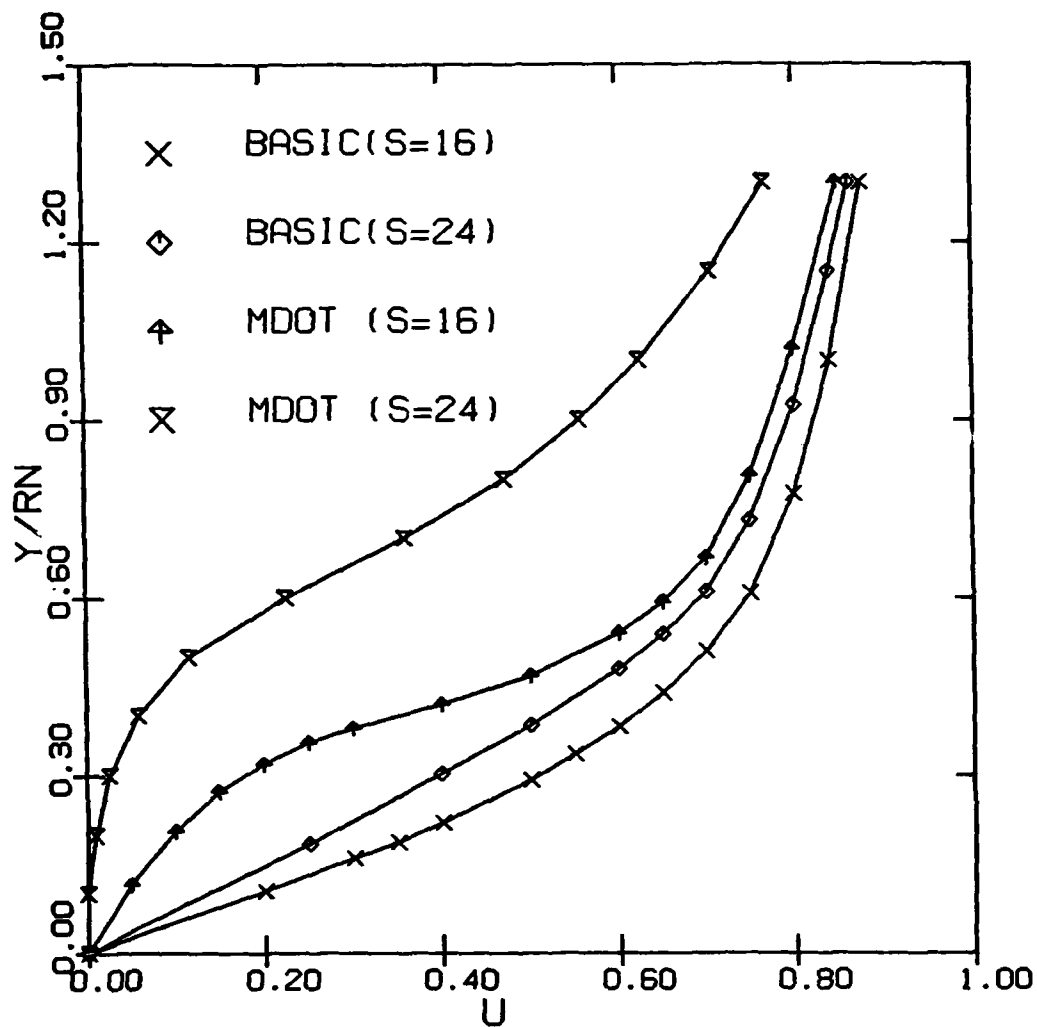


Figure 18: Case 1a Effect of mass transfer on the axial flow separation.

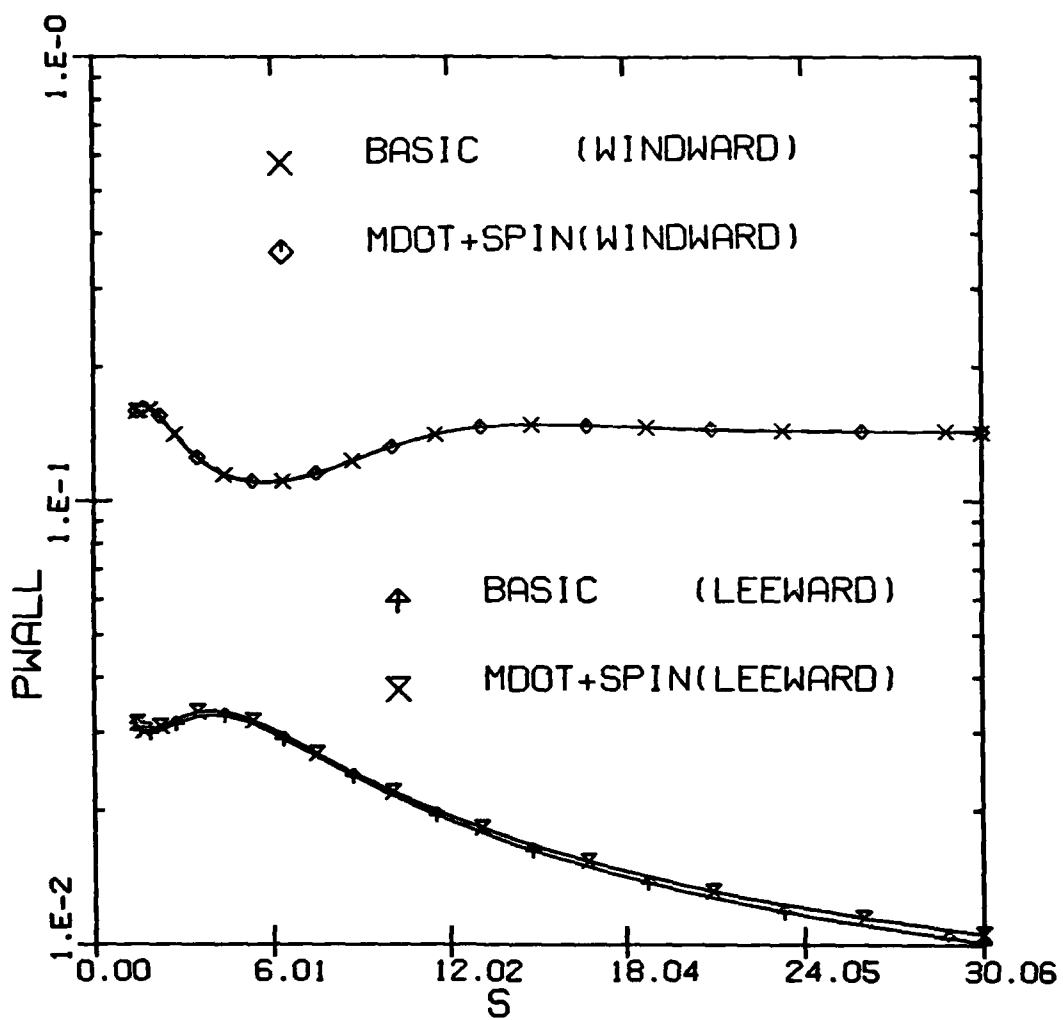


Figure 19: Case 2 Effects of mass transfer and spin on the surface pressure along the body.

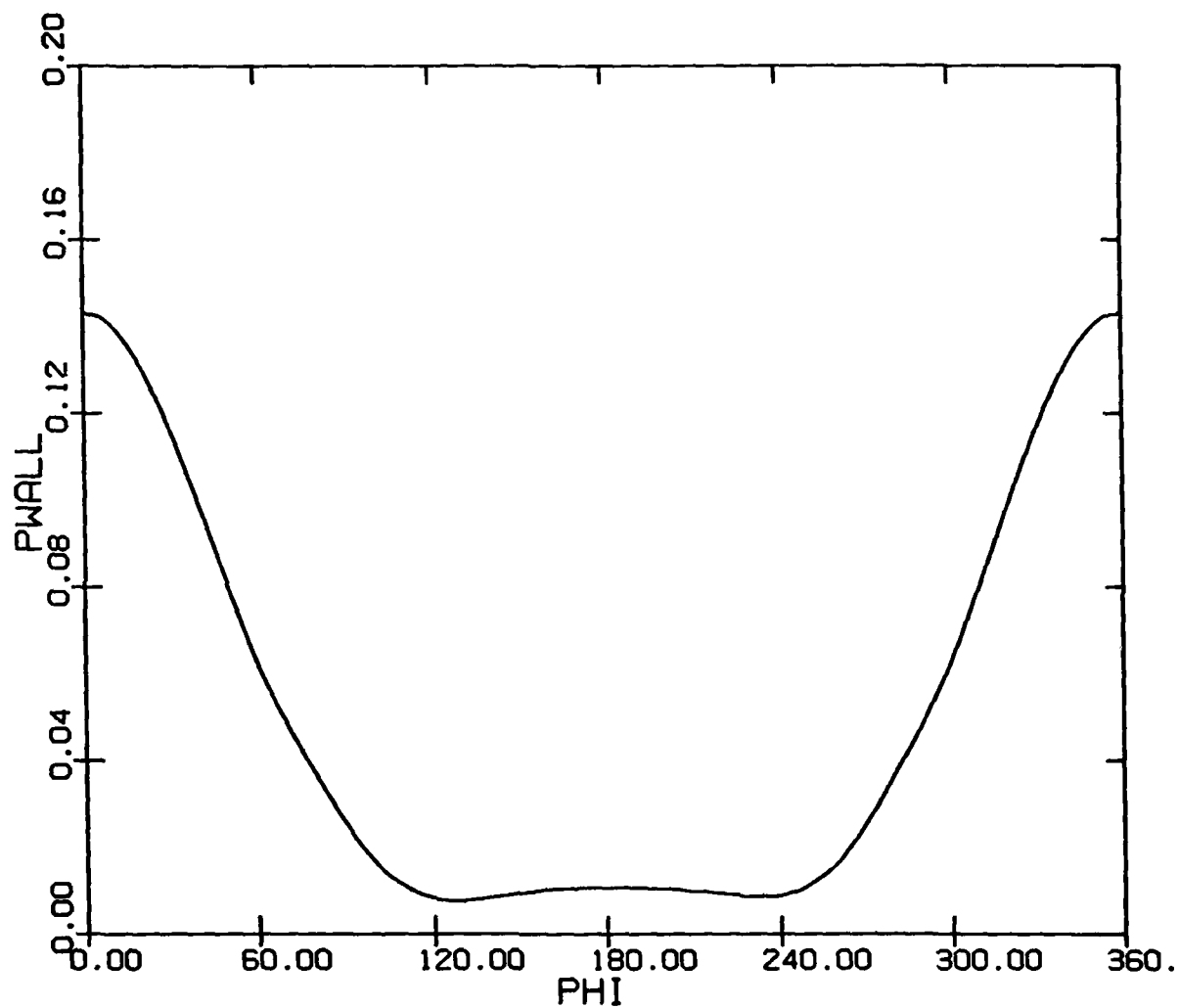


Figure 20: Case 2 Surface pressure around the body with mass transfer and spin at $s = 30.06$.

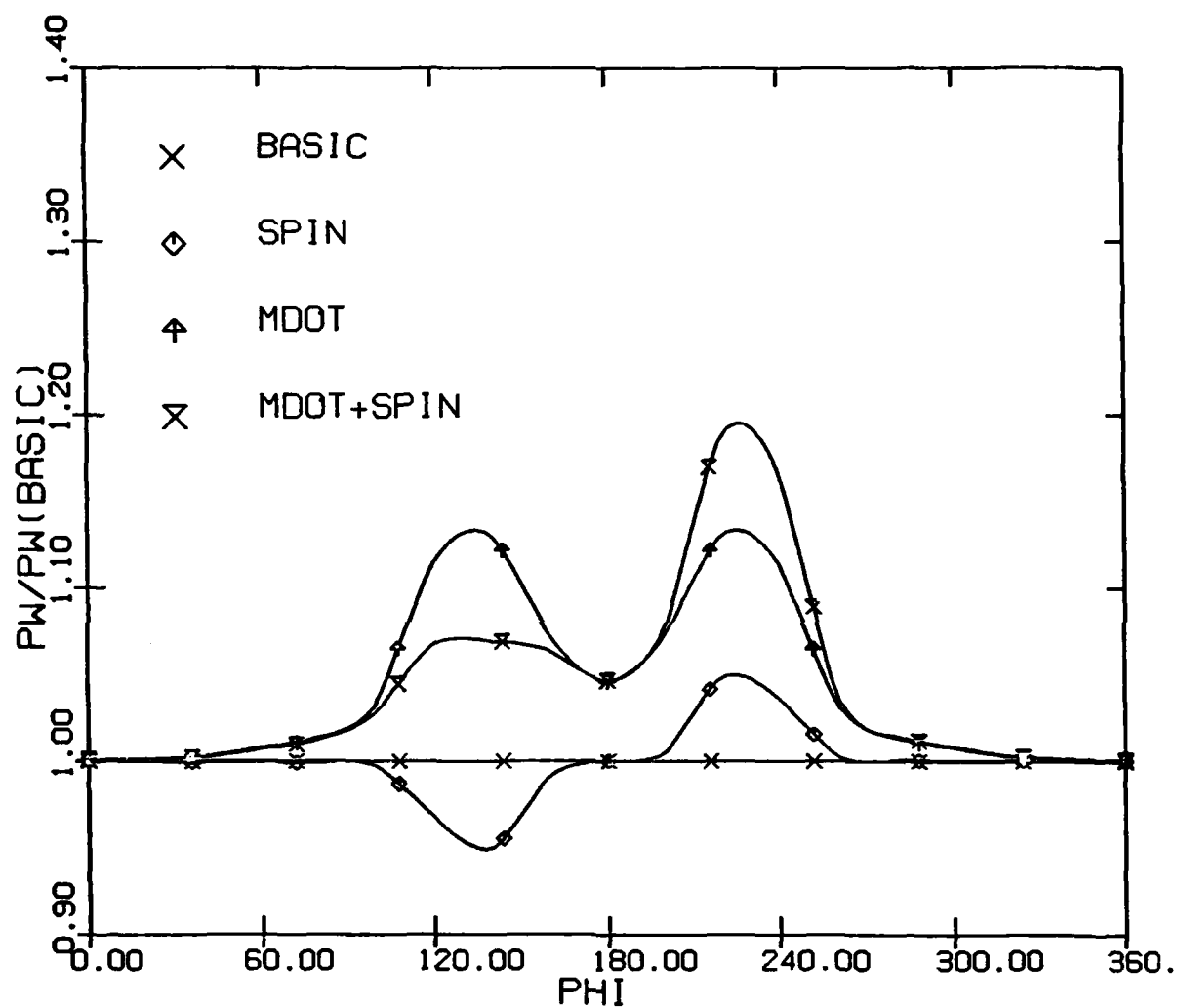


Figure 21: Case 2 Effects of mass transfer and/or spin on the surface pressure around the body at $s = 30.06$.

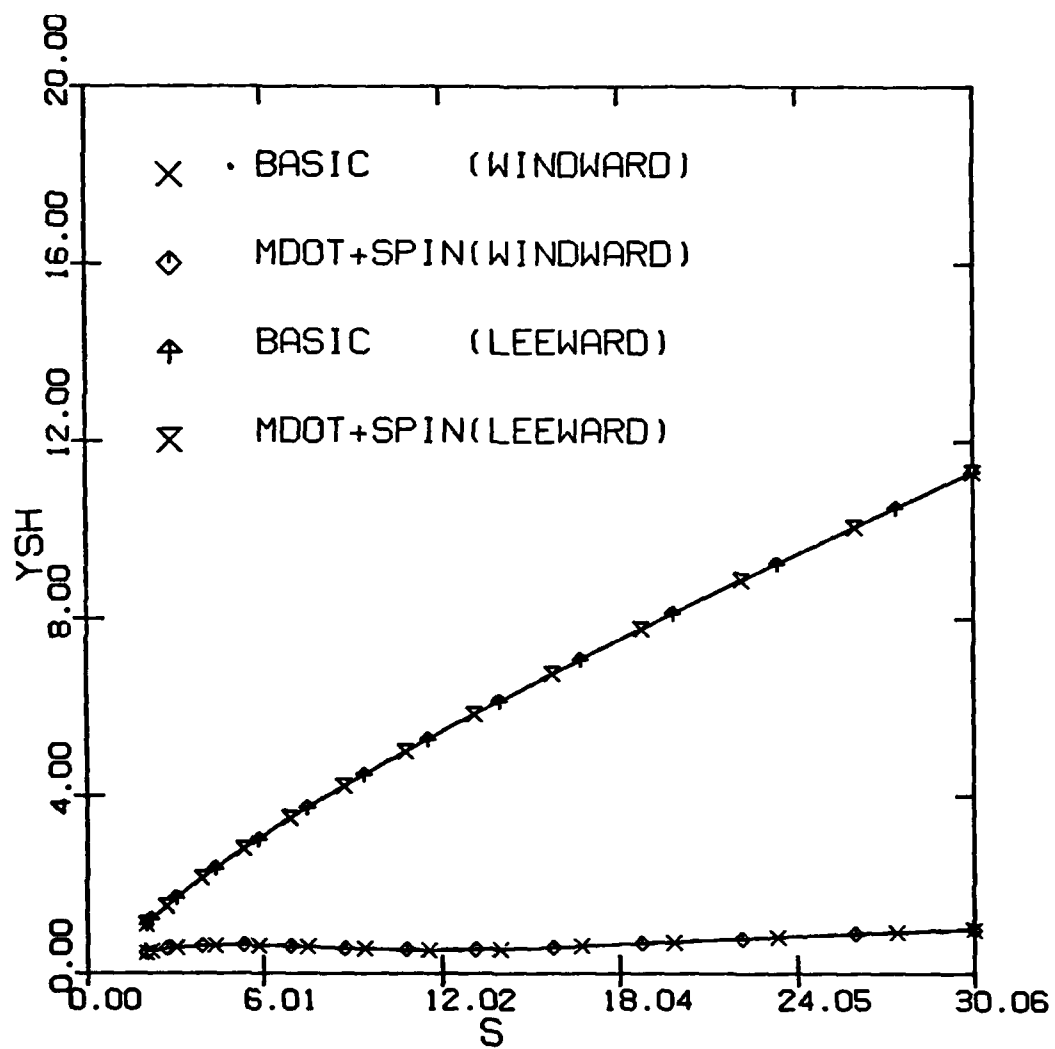


Figure 22: Case 2 Effects of mass transfer and spin on the shock-layer thickness along the body.

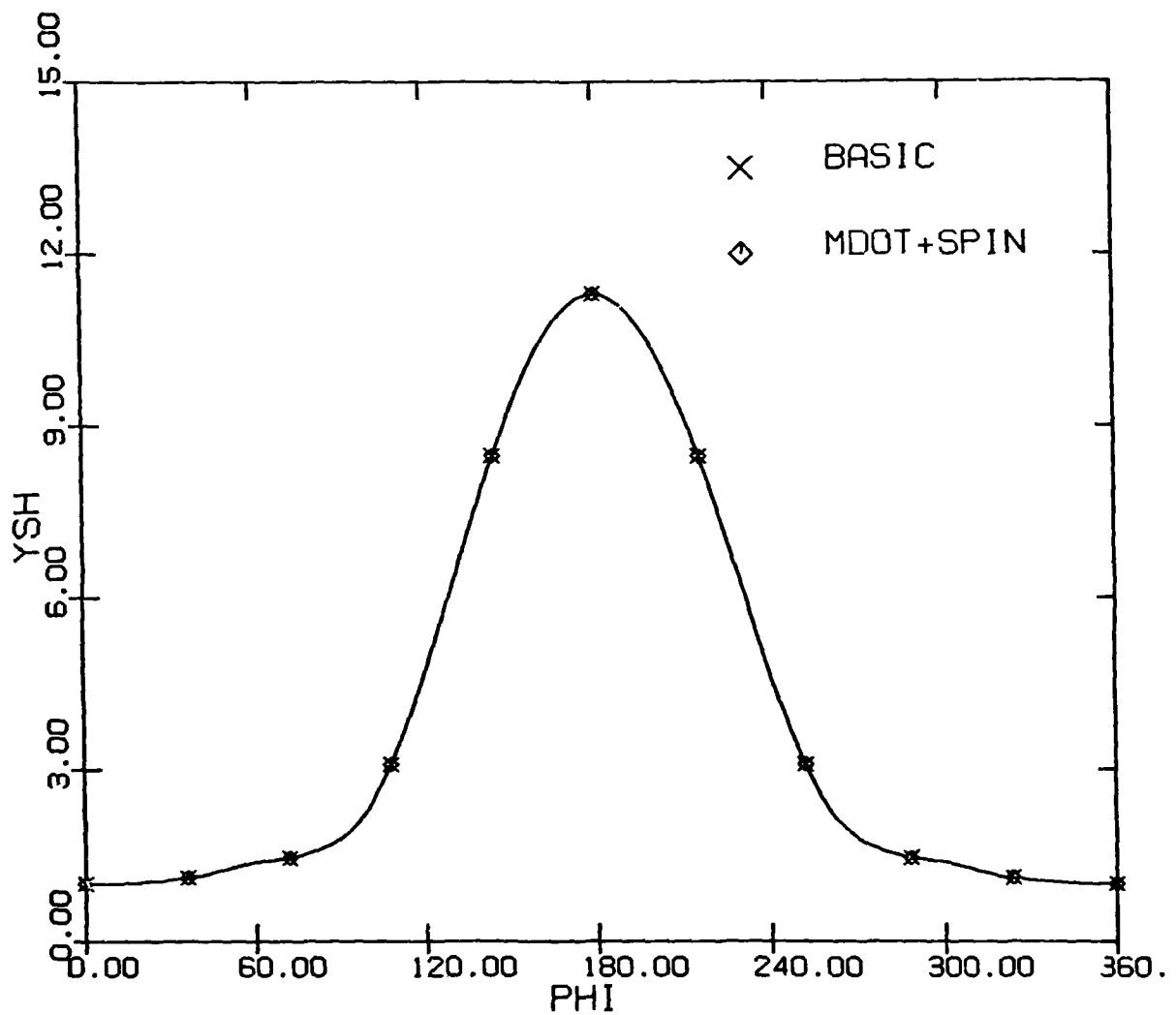


Figure 23: Case 2 Effects of mass transfer and spin on the shock-layer thickness around the body at $s = 30.06$.

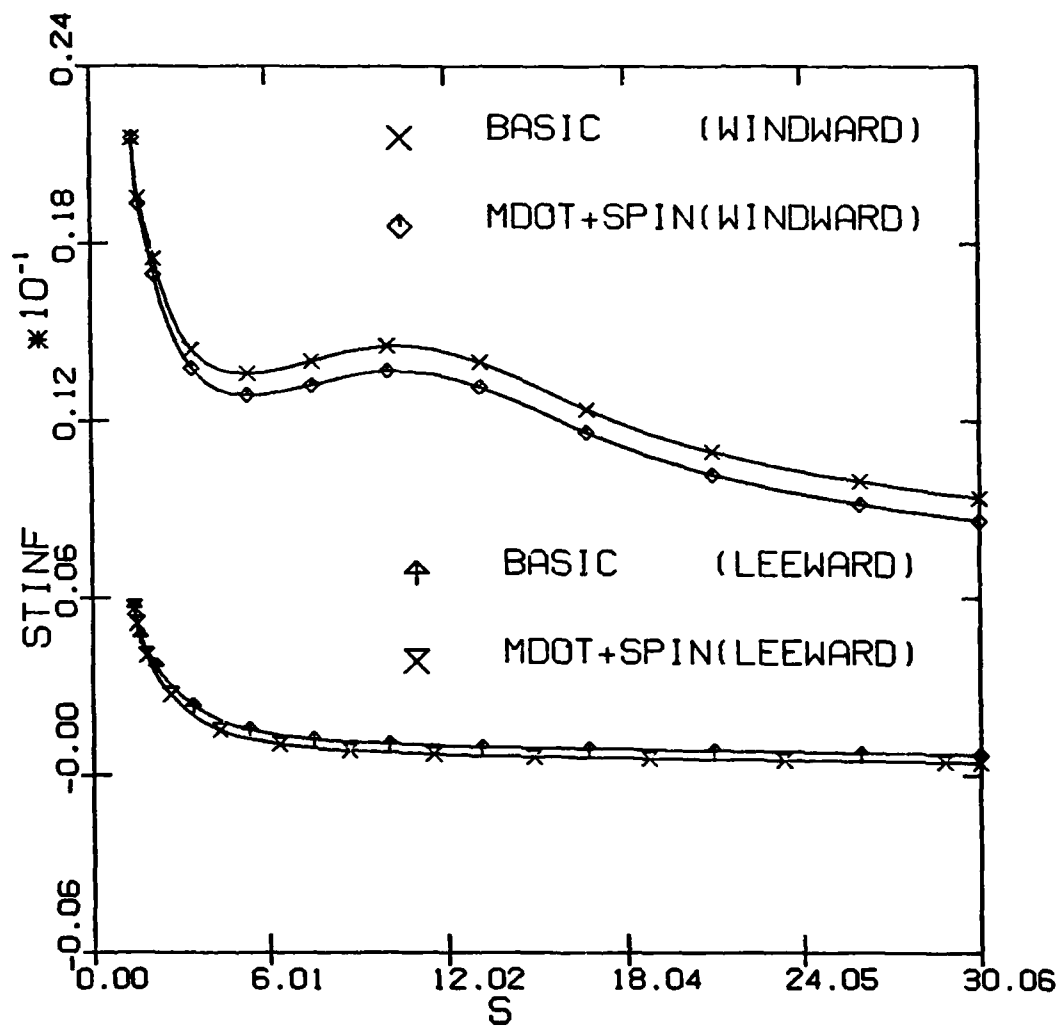


Figure 24: Case 2 Effects of mass transfer and spin on the heat transfer along the body.

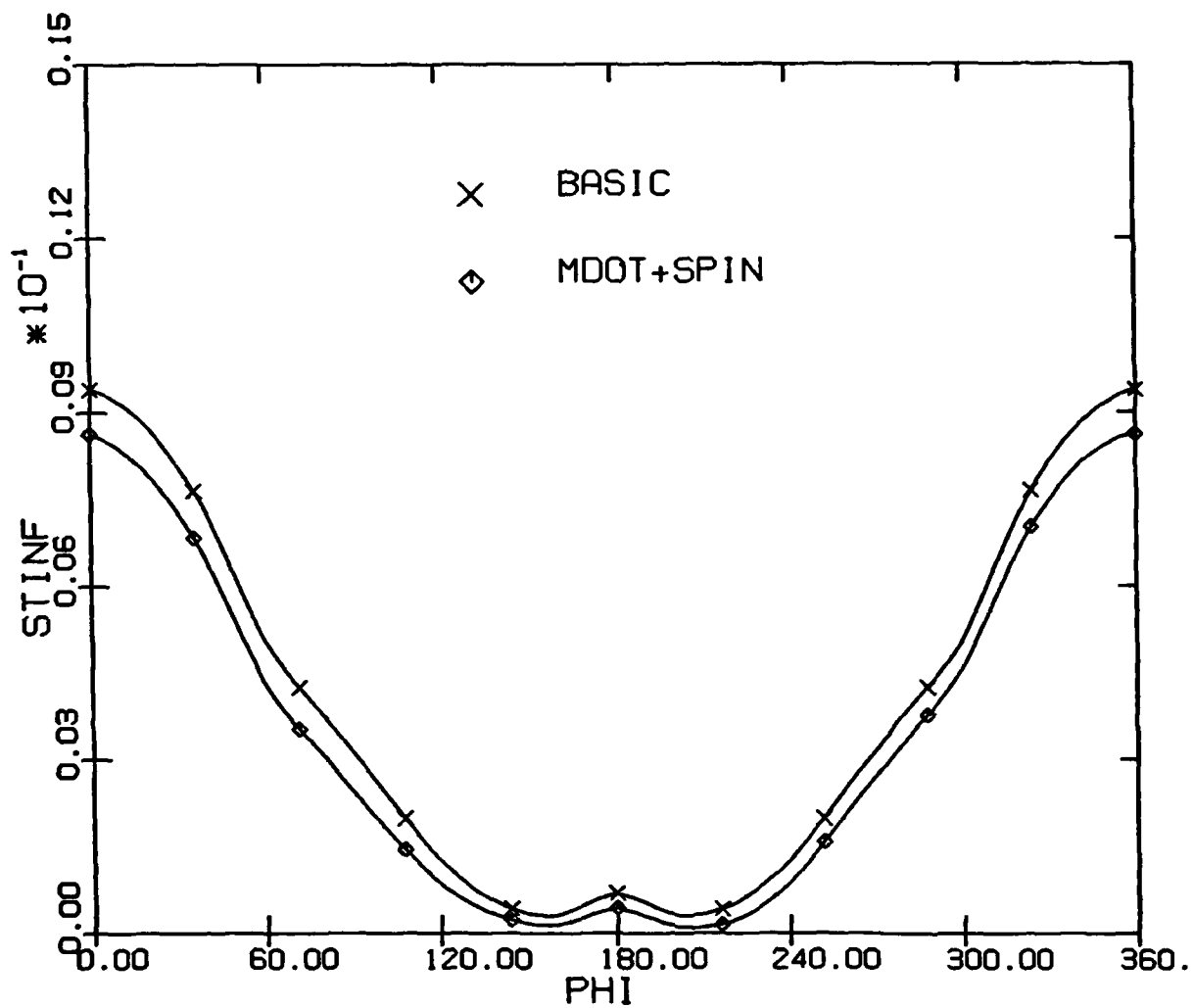


Figure 25: Case 2 Effects of mass transfer and spin on the heat transfer around the body at $s = 30.06$.

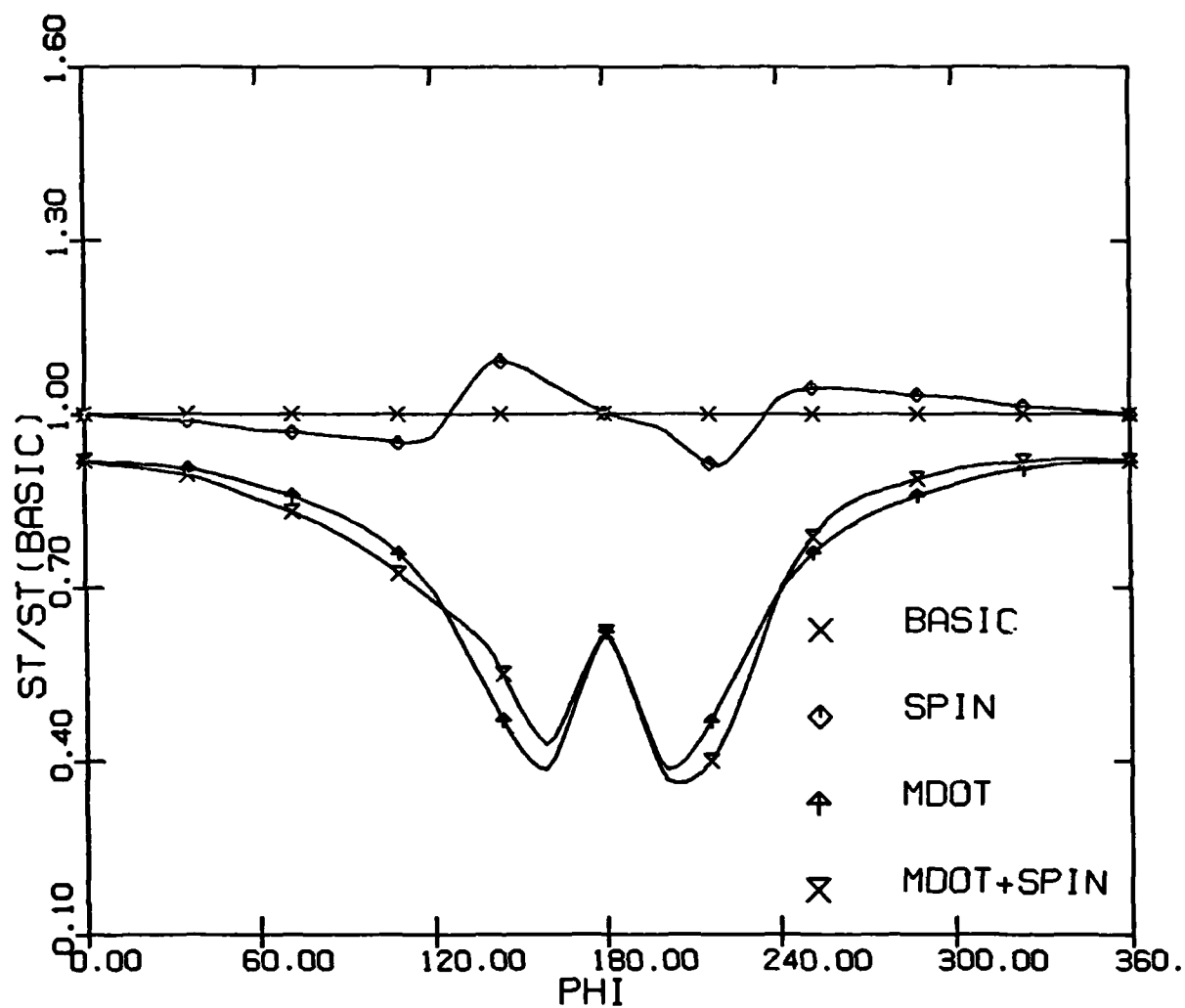


Figure 26: Case 2 Effects of mass transfer and/or spin on the heat transfer around the body at $s = 30.06$.

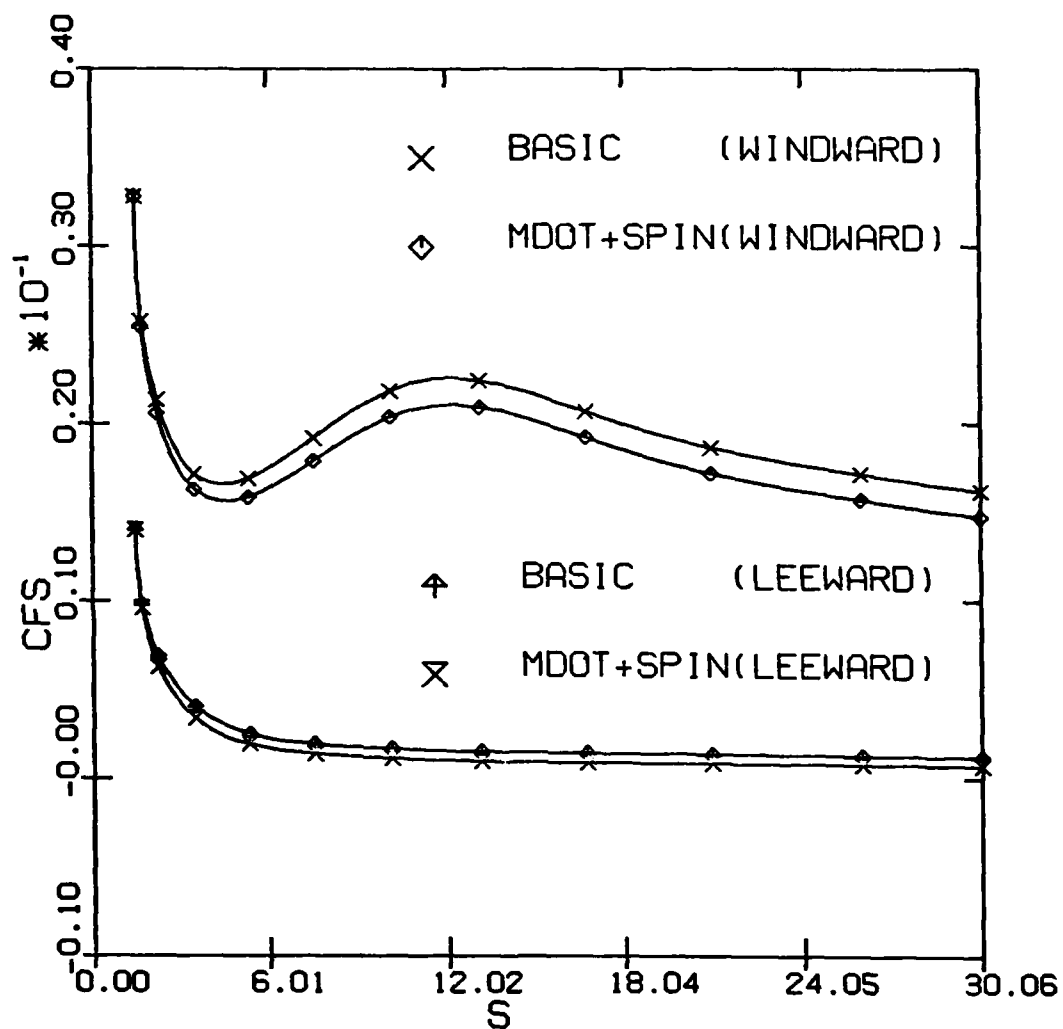


Figure 27: Case 2 Effects of mass transfer and spin on the streamwise shear along the body.

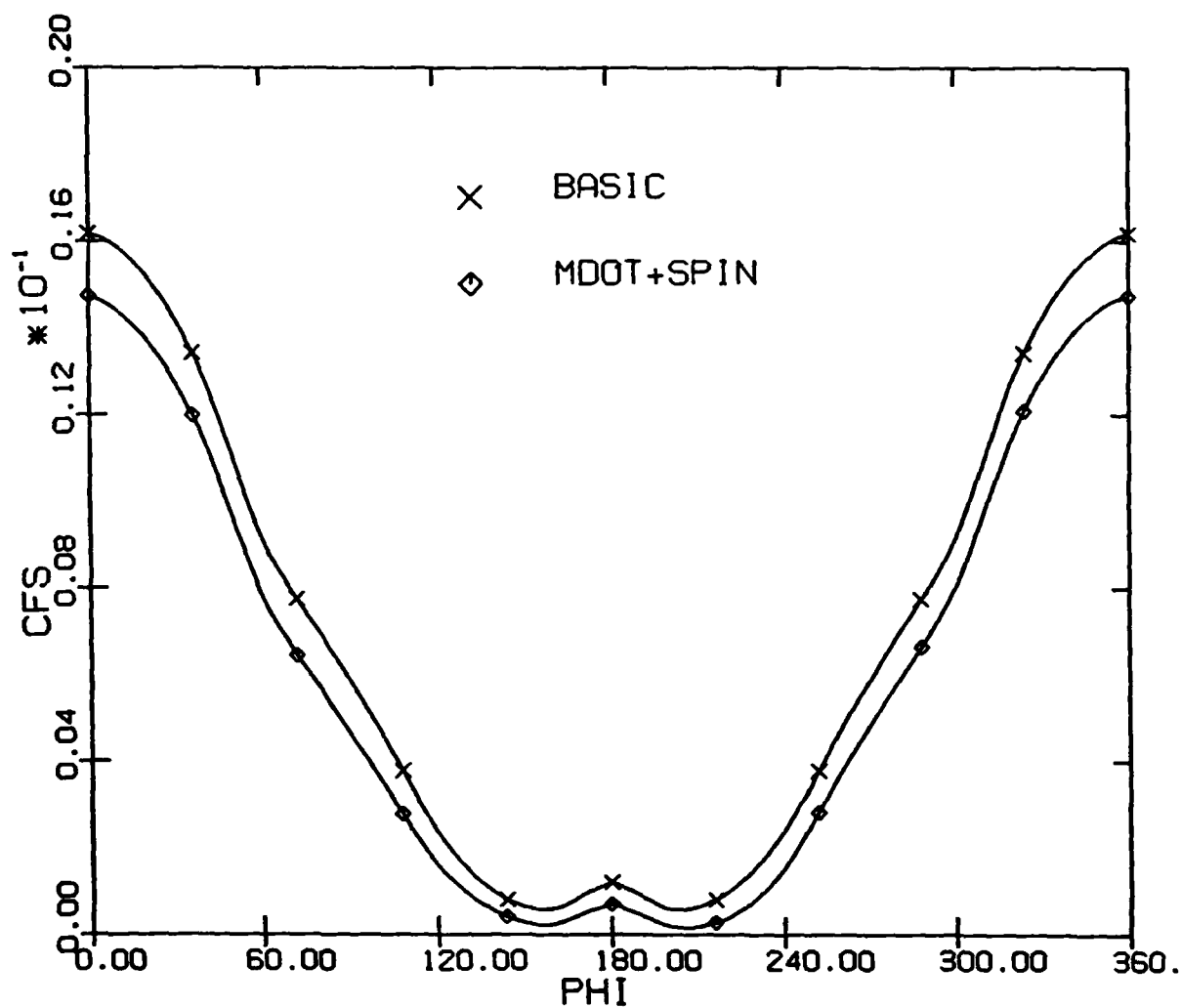


Figure 28: Case 2 Effects of mass transfer and spin on the streamwise sheat around the body at $s = 30.06$.

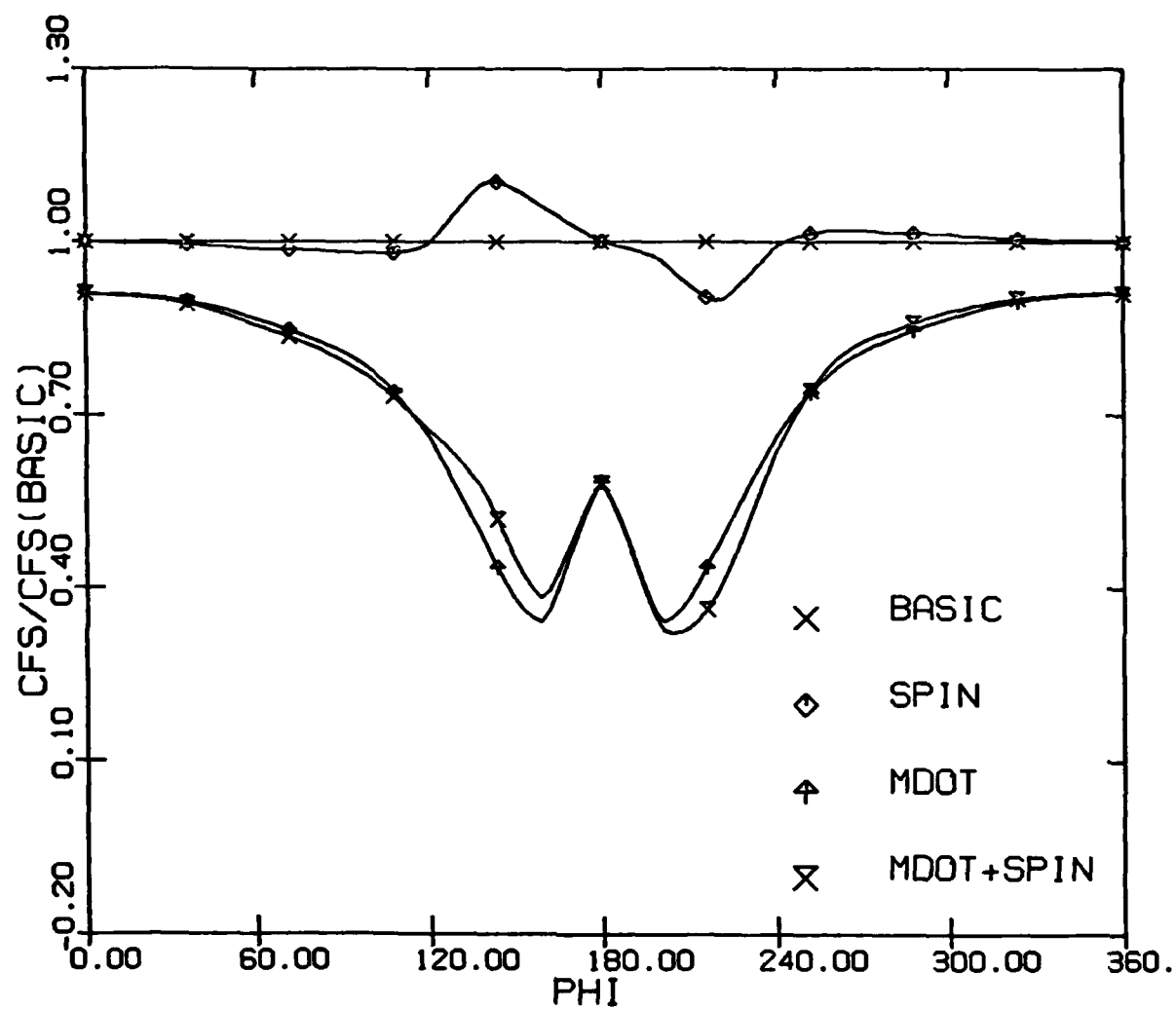


Figure 29: Case 2 Effects of mass transfer and/or spin on the streamwise shear around the body at $s = 30.06$.

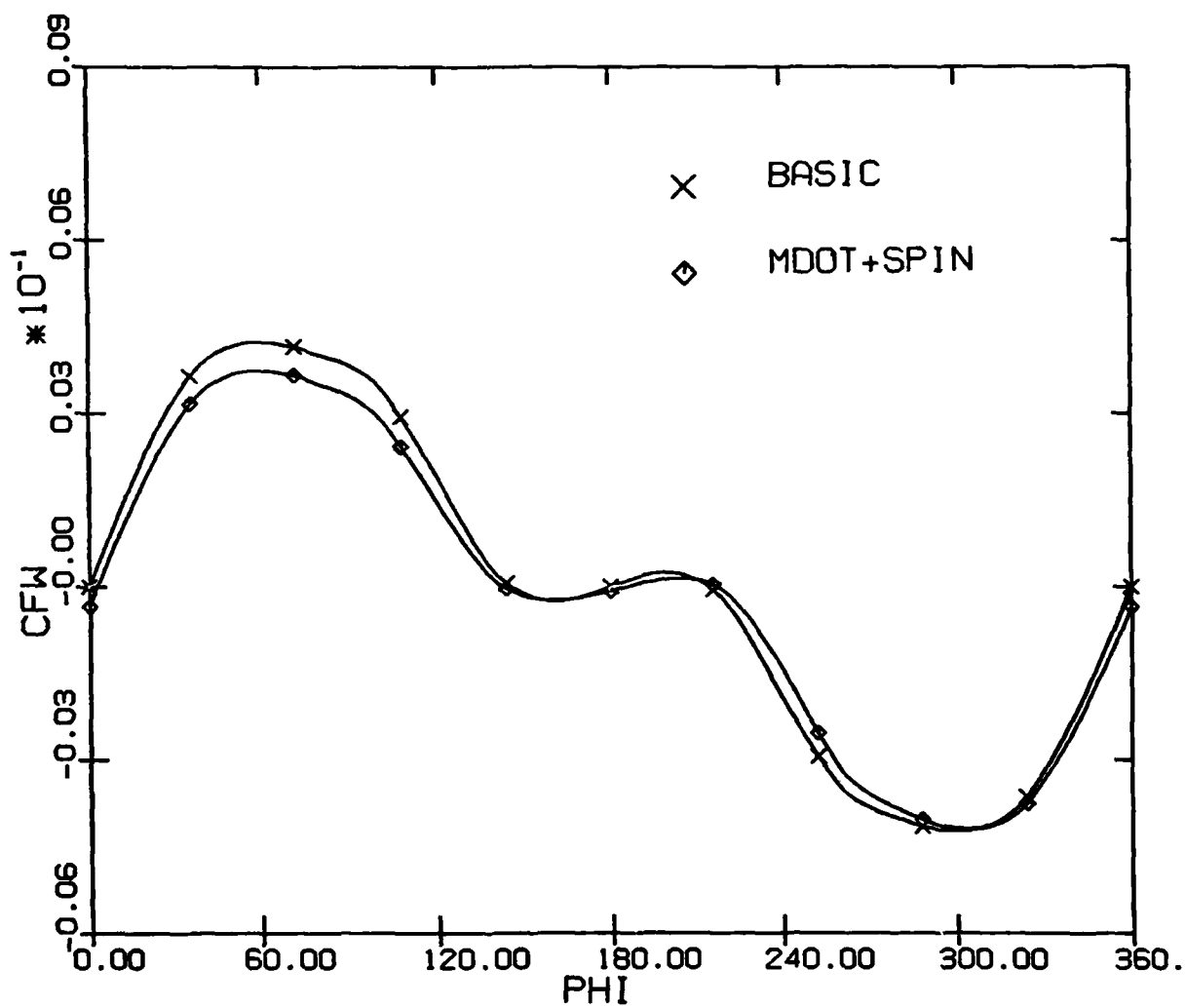


Figure 30: Case 2 Effects of mass transfer and spin on the crossflow shear around the body at $s = 30.06$.

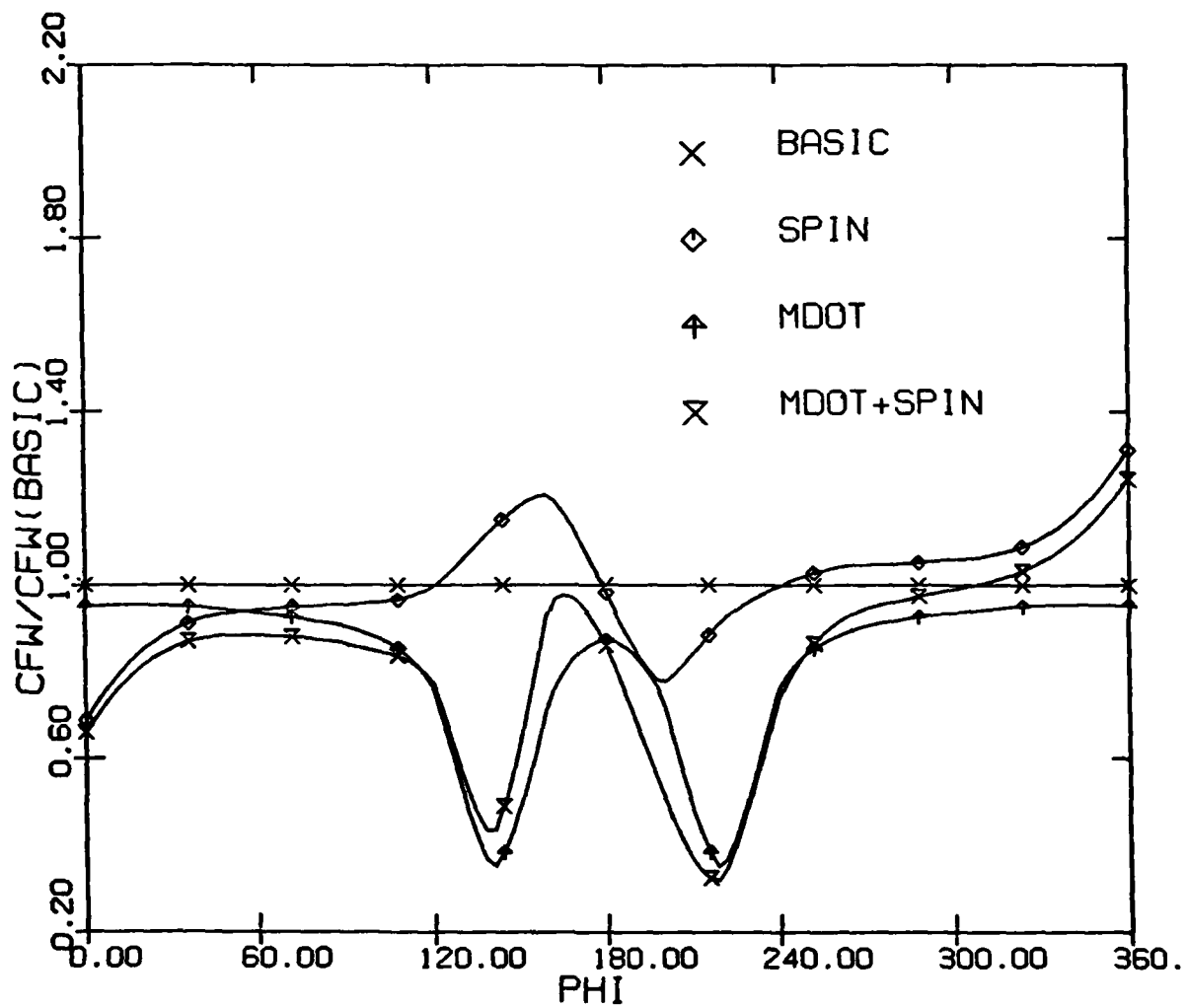


Figure 31: Case 2 Effects of mass transfer and/or spin on the crossflow shear around the body at $s = 30.06$.

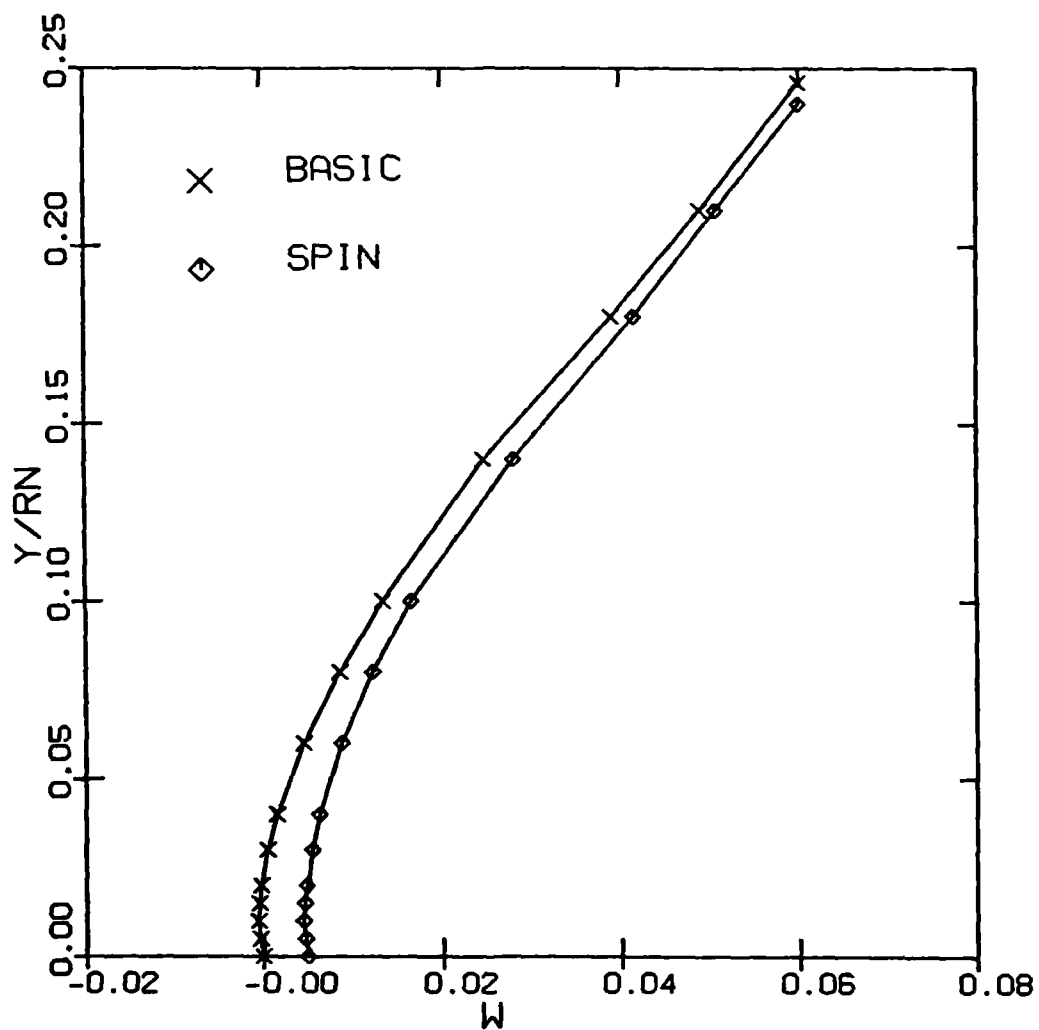


Figure 32: Case 2 Effect of spin on the crossflow velocity at $s = 6.40$, $\phi = 160$ deg

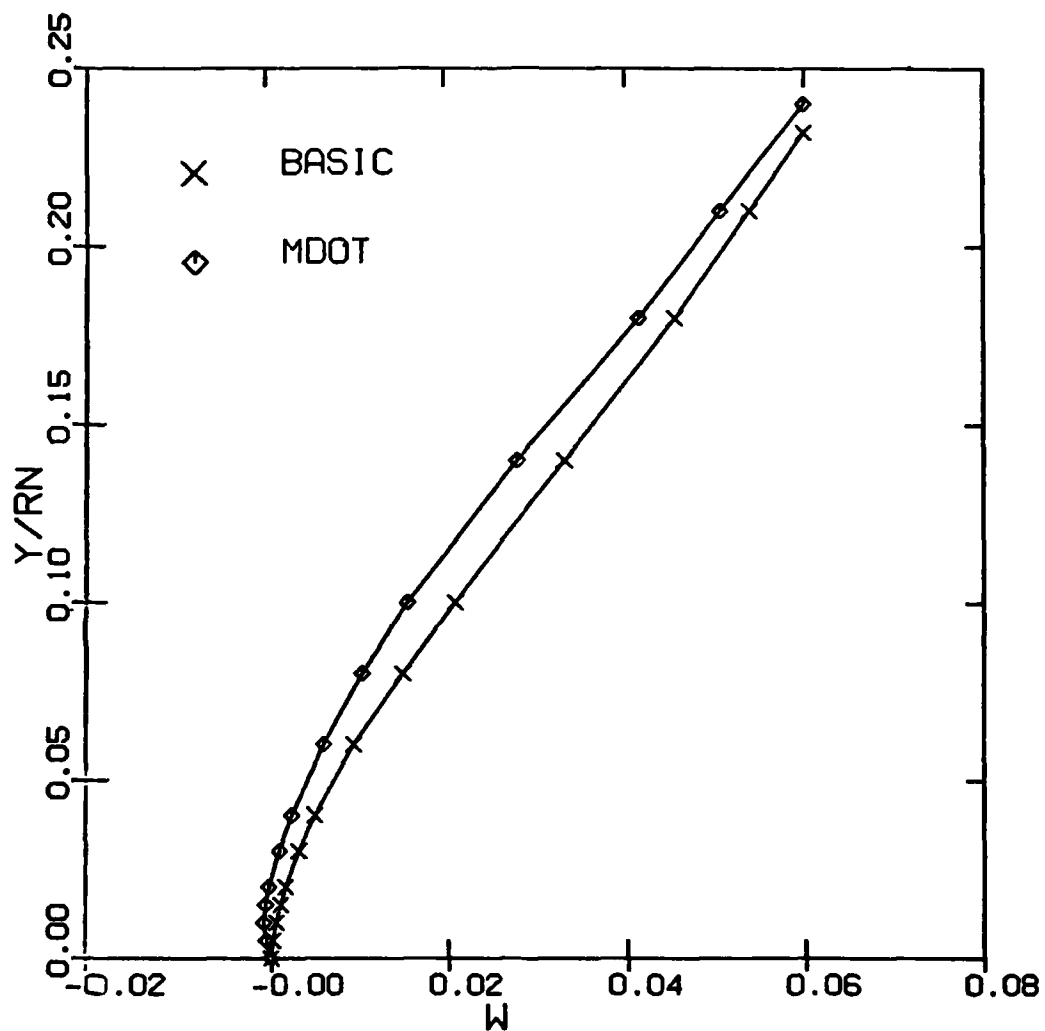


Figure 33: Case 2 Effect of mass transfer on the crossflow velocity at $s = 5.85$, $\phi = 160$ deg.